AN EXPERIMENTAL STUDY OF SURFACE PRESSURE
FLUCTUATIONS IN A SEPARATING TURBULENT
BOUNDARY LAYER

Roger L. Simpson, M. Ghodbane,
and B. E. McGrath

VIRGINIA POLYTECHNIC INSTITUTE AND STATE UNIVERSITY
Blacksburg, Virginia

NASA

National Aeronautics and
Space Administration

Langley Research Center
Hampton, Virginia 23665

SUMMARY

Measurements of streamwise velocity fluctuation and surface pressure
fluctuation spectra and wavespeeds are reported for a well-documented
separating turbulent boundary layer. A two-parallel-wire hot-wire anemom-
eter probe was used to measure the velocity fluctuations while two sensi-
tive instrumentation microphones were used to measure pressure fluctuations
through pinhole apertures in the flow surface. Because a portion of the
acoustic pressure fluctuations are the same across the nominally two-
dimensional turbulent flow, it is possible to decompose the two microphone
signals and obtain the turbulent flow contributions to the surface pressure
spectra.

The velocity spectra and wavespeeds behave as expected with the spectrum
function $F(n) \sim n^{-1}$ near the wall upstream of detachment and $F(n) \sim n^{-5/3}$
in the higher frequency inertial subrange. The wavespeed or celerity
increases at low frequencies to the local mean velocity at high frequencies,
as observed by Strickland and Simpson (1973) for a separating turbulent
boundary layer.

The rms surface pressure fluctuation p' increases monotonically
through the adverse pressure gradient attached flow region and the detached
flow zone. Apparently $\overline{p^2}$ is proportional to the ratio of streamwise length
scale to length scales in other directions α. For non-equilibrium
separating turbulent boundary layers, α is as much as 2.5, causing $\overline{p^2}$ to
be higher than equilibrium layers with lower values of α.

The maximum turbulent shearing stress τ_M appears to be the proper
stress on which to scale p' ; p'/τ_M from available data shows much less

variation than when p' is scaled on the wall shear stress. In the present
measurements p'/τ_M increases to the detachment location and decreases
downstream. This decrease is apparently due to the rapid movement of the
pressure-fluctuation-producing motions away from the wall after the begin-
ning of intermittent backflow. A correlation of the detached flow data is
given.

The spectra $\phi(\omega)$ correlate well when normalized on the maximum
shearing stress τ_M. At lower frequencies for the attached flow $\phi(\omega) \sim \omega^{-0.7}$
while $\phi(\omega) \sim \omega^{-3}$ at higher frequencies in the strong adverse pressure
gradient region. After the beginning of intermittent backflow, $\phi(\omega)$ varies
with ω at low frequencies and ω^{-3} at high frequencies; farther downstream
the lower frequency range varies with $\omega^{2.4}$.

The celerity of the surface pressure fluctuations for the attached
flow increases with frequency as suggested by other measurements and
agrees with the semi-logarithmic overlap equation of Panton and Linebarger.
After the beginning of the separation process, the wavespeed decreases
because of the oscillation of the instantaneous wavespeed direction. The
streamwise coherence decreases drastically after the beginning of flow
reversal.

TABLE OF CONTENTS

NOMENCLATURE

c	speed of sound, mps
d	diameter of microphone, m
$F(k), F(n)$	spectrum function of k or n; $\int_0^\infty F(n)dn = \int_0^\infty F(k)dk = 1$
H	δ^*/θ, velocity profile shape parameter
K	damping constant in equation (28)
k	$= 2\pi/\lambda$ wavenumber, m^{-1}
L	length scale in equation (25), m
N	distance from wall to maximum shear stress location, m
n	frequency, Hz
P,p	mean and fluctuation wall pressures, Pa
p'	rms wall pressure fluctuation, Pa
q	dynamic pressure, Pa
$\vec{R}$	position vector, m
R_n	correlation coefficient for frequency n
S	length of detached flow zone, m
U,V,W	mean velocities in X,Y, Z directions, mps
u,v,w	fluctuation velocities in X,Y, Z directions, mps
$\overline{u^2}, \overline{v^2}, \overline{w^2}$	mean square velocity fluctuations, $(mps)^2$
$-\overline{uv}$	kinematic Reynolds shear stress, $(mps)^2$
U_M, U_τ	$\sqrt{\dfrac{\tau_M}{\rho}}, \sqrt{\dfrac{\tau_W}{\rho}}$, shear velocities based on maximum and wall shear stresses, mps
U_{cn}, U_{cn}	$\dfrac{\omega}{k}, \dfrac{\overline{\omega}}{k}$ instantaneous and mean celerities or wavespeeds at frequency n, mps
$\dot{U}_s$	Perry and Schofield velocity profile scale, mps
X,Y,Z	streamwise, normal to wall, spanwise positions, m
$\Delta X, \Delta Y, \Delta Z$	spacing of sensors in streamwise, normal to wall, spanwise directions, m

Greek Symbols

α — ratio of streamwise length scale to length scales in other directions

γ^2 — coherence function, $|G_{XY}|^2/G_{XX}G_{YY}$

γ — square root of the coherence function

Δ — Perry and Schofield length scale, m

δ, δ^*, θ — boundary layer, displacement and momentum thicknesses, m

κ — von Kármán constant

ν — kinematic viscosity, m^2/S

Π — Coles wake function parameter

ρ — density, kg/m^3

τ — shearing stress, Pa

$\Phi(\omega)$ — spectrum function, $p'^2 = \int_{-\infty}^{+\infty} \phi(\omega)d\omega$

ϕ — phase

ω — $2\pi n$, angular frequency, rad/S

Subscripts

i,j — tensor directions

n — value associated with frequency n

ref — reference inlet value

∞ — local freestream condition at outer edge of boundary layer

I. INTRODUCTION

Noise generated by helicopter and turbomachine rotors is a nuisance that designers would like to predict and to minimize within other design constraints. Brooks and Schlinker (1983) reviewed some recent research on helicopter rotor noise and discussed the categories of noise sources, which include blade self-noise generation by strong adverse-pressure-gradient attached turbulent boundary layers and by separated turbulent boundary layers that accompany stall.

Brooks and Hodgson (1981) showed that starting with given surface pressure fluctuation spectra and convective speeds, radiated noise due to the turbulent boundary layer can be predicted. Furthermore, if the surface pressure fluctuation spectra and convective speeds can be related to the turbulent flow structure, then turbulent boundary layer flowfield calculation methods can be used when designing rotors to estimate the needed surface pressure fluctuation information.

Thus, a key requirement for this noise calculation procedure is knowledge relating the flowfield structure to the surface pressure fluctuation structure. Unfortunately there are few measurements of both flowfield structure and surface pressure fluctuation structure for a given flow, especially in the presence of adverse pressure gradients. Only recently have detailed flowfield measurements been made of a nominally two-dimensional, steady freestream, separated turbulent boundary layer (Simpson et al., 1981, a, b, c). This report presents information on the surface pressure fluctuations for this well-documented velocity flowfield.

1

After discussing some previous work on surface pressure fluctuations for zero and adverse-pressure-gradient and separating turbulent boundary layer flows in the next section, a review of the test wind tunnel and a summary of the nature of this separating turbulent boundary layer flowfield are given. In following sections the experimental instrumentation, techniques and results are discussed for the streamwise velocity spectra and celerities and the surface pressure fluctuation spectra and celerities.

II. SOME PREVIOUS WORK ON SURFACE PRESSURE FLUCTUATIONS

First, it should be stated at the beginning that static pressure fluctuations can only be measured non-intrusively at the wall in a turbulent boundary layer. Small pinhole openings in the surface have been used to measure fluctuations with microphones. Small piezoelectric transducers flush with the surface have also been used to avoid any influence of a pinhole on the flow. Sufficiently small sensing surfaces must be used to pick up small scale fluctuations. Flow disturbances are present in most wind tunnels, so measurements of the low frequency components of the wall pressure fluctuations are impossible to make with a single sensor. Willmarth (1975) reviewed many measurements, pointing out the shortcomings of each set of available data. Needless to say, there are significant differences between results obtained for approximately the same flow conditions by different investigators.

As in all other practical turbulent flow problems, purely theoretical calculations of surface pressure fluctuations have not yet been done successfully. In incompressible turbulent flow the fluctuating

pressure p is related to the velocity fluctuations by the Poisson equation

$$\frac{\partial^2 p}{\partial x_i^2} = - \rho q \tag{1}$$

where the source term q is given in tensor notation by

$$q = 2 \frac{\partial U_i}{\partial x_j} \frac{\partial u_j}{\partial x_i} + \frac{\partial^2}{\partial x_i \partial x_j} (u_i u_j - \overline{u_i u_j}) \tag{2}$$

and U_i and u_i are the mean and fluctuation velocity components in the x_i direction. The first term on the right side of this equation represents the turbulence-mean shear interaction while the second term represents the turbulence-turbulence interaction. For a wall-bounded flow, if contributions from surface integrals are neglected, then the fluctuating pressure at a point $\vec{X}$ on the wall is given by

$$p(\vec{X}) = \frac{\rho}{2\pi} \int_{Y > 0} \frac{q(\vec{R}_s) \, dV \, (\vec{R}_s)}{(\vec{X} - \vec{R}_s)} \tag{3}$$

where the volume integration is at position $\vec{R}_s$ over the entire half-space containing the flow. This equation indicates that while surface pressure fluctuations are produced from sources in a large region of the flow, contributions from various sources drop off rapidly with their distance from the point under consideration. Although several attempts have been made to calculate p from equation (3), Willmarth (1975) pointed out that it appears that such efforts suffer from the lack of accurate information about the fluctuating velocity field within the boundary layer. Consequently, the effects of adverse pressure gradients and separation on surface pressure fluctuations as suggested by calculations

are uncertain and need confirmation by experimental data.

Panton and Linebarger (1974) calculated wall pressure spectra for zero pressure gradient and adverse pressure gradient equilibrium boundary layers that seem to describe the essential features observed from experiments. They used Coles' laws of the wall and wake for the mean velocity profiles. A scale-anisotropic model of the spatial correlation of v was used together with the assumption that v was proportional to $(-\overline{uv})^{1/2}$. As in some earlier calculations, only the turbulence-mean shear interaction was modeled since the turbulence-turbulence interaction contributes only a very small portion to the mean-square value.

Their spectral results showed larger contributions at higher Reynolds numbers for $k\delta < 20$. The contributions to the spectrum at these low frequencies are due to the outer region velocity and turbulence structure and depend upon the pressure gradient. An overlap region between the low frequency outer region contributions and the high-frequency near-wall viscous-dominated part of the spectrum varies with k^{-1}, as shown by Bradshaw (1967) using dimensional analysis. For this overlap region, their calculation results can be approximated by

$$\frac{kF(k)}{\tau_w^2} \approx 1.73\ (\alpha)^{0.9} \quad \text{for} \quad \frac{k\nu}{U_\tau} < 0.06 \tag{4}$$

Here α is the ratio of the streamwise length scale to length scales in other directions, which strongly influences the spatial correlation of v. At higher frequencies

$$\frac{kF(k)}{\tau_w^2} = 0.0173 \left(\frac{k\nu}{U_\tau}\right)^{-2} \quad \text{for } \frac{k\nu}{U_\tau} \geq 0.1 \tag{5}$$

Note that these two equations are independent of Reynolds number and are scaled on the wall shearing stress.

Because the low frequency part of the spectrum is Reynolds number dependent, the mean square pressure fluctuation increases with Reynolds number. The equation

$$\frac{\overline{p^2}}{\tau_w^2} = 0.52 \; \alpha^{0.9} \; (\ell n \; / \; \frac{U_\tau \delta}{\nu} \; / \; + \; 9.24) \tag{6}$$

fits Panton and Linebarger's calculations for a zero pressure gradient with $\alpha = 1$, 2 and 3, and a Coles' wake function parameter $\Pi = 0.6$. In terms of the displacement thickness Reynolds number

$$\frac{U_\tau \delta}{\nu} = \frac{K}{1+\Pi}\left(\frac{U_\infty \delta^*}{\nu} - 65\right) \tag{7}$$

(Coles and Hirst, 1969).

The spectral measurements of Bull and Thomas (1976) showed that zero pressure gradient flow measurements with a pinhole microphone, such as Blake's (1970), are too high for frequencies higher than the high frequency end of the overlap region, $\omega\nu/U_\tau^2 > 0.1$. This effect extends to $\omega\nu/U_\tau^2 > 2$. The pinhole microphone interacts with the viscous flow to amplify the frequencies in this range. The spurious amplification appears to be a function of $\omega\nu/U_\tau^2$ for the narrow range of test parameters that were used. Bull (1967), Lim (1971) and Schloemer (1967) used flush-surface piezoelectric pressure transducers that were relatively large so high frequency contributions to the mean square pressure fluctuation

were attenuated (Willmarth, 1975). Consequently, the rms pressure fluctuations were too low for these latter measurements, as shown in Figure 1.

The spectral measurements of Bull and Thomas (1976) show a short $\Phi(\omega) \sim \omega^{-1}$ region ($0.05 < \omega\nu/U_\tau^2 < 0.2$) and a higher frequency $\Phi(\omega) \sim \omega^{-3}$ region ($\omega\nu/U_\tau^2 > 0.5$). Their rms pressure fluctuation measurements with a piezoelectric transducer are still slightly too low because the sensing diameter was too large ($44 < dU_\tau/\nu < 65$) to pick up the smallest scale turbulent motions ($\lambda_z U_\tau/\nu \approx 12$). Thus the p'/τ_w values calculated by Panton and Linebarger for the zero-pressure-gradient case appear to be approximately correct.

At the lower frequencies of the overlap region, the pressure fluctuation spectrum for the zero-pressure-gradient case scales on the outer variables U_∞ and δ^*. The spectral level seems to be almost the same in various investigations with

$$10 \log_{10} \left| \frac{\Phi(\omega)U_\infty}{q_\infty^2 \delta^*} \right| = -51 \pm 2 \quad \text{at } \omega\delta^*/U_\infty = 1 \qquad (8)$$

(Bull and Thomas, 1976; Burton, 1973; Willmarth, 1975; Schloemer, 1966; Panton and Linebarger, 1974). For $0.1 < \omega\delta^*/U_\infty < 1$, $\Phi(\omega)$ levels off and is about constant in most investigations. For the lowest measureable frequencies, $\Phi(\omega)$ generally increases slightly with ω, although there is some scatter in data due to different low frequency disturbances in different test wind tunnels.

For adverse-pressure-gradient equilibrium turbulent boundary layers, the low frequency part of the spectrum ($k\delta < 20$) scales approximately on
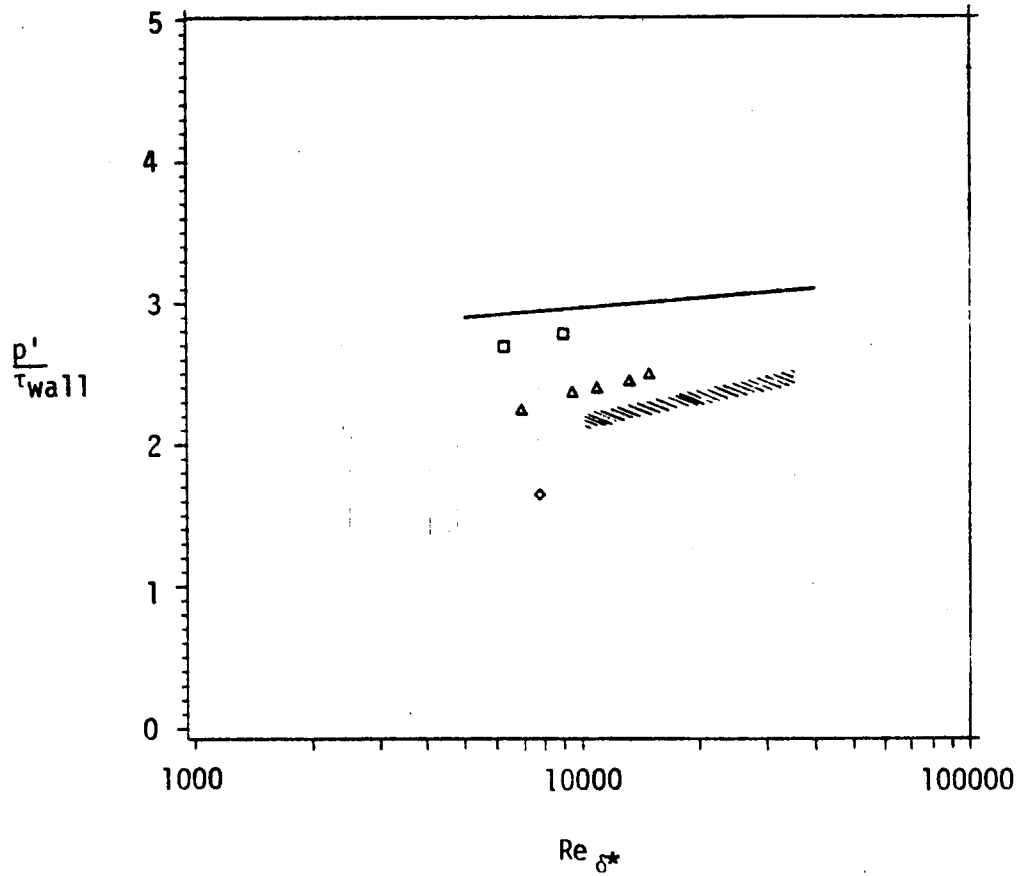
Figure 1: p'/τ_{wall} for some zero pressure gradient experiments.
Solid lines: Panton and Linebarger, $\alpha=1.0$ and $\pi=0.6$ (1974);
□: Bull and Thomas (1976); △: Lim (1971); ◇: Schloemer;
Shaded region: Bull (1967) and Willmarth (1958).

the maximum shearing stress in the boundary layer (Mabey, 1982). This can be seen in Figure 10 of Panton and Linebarger (1974) for $\pi = 1.5$, 3, and 6, together with the maximum shearing stress estimated from

$$\frac{\tau_M}{\rho U_\infty^2} = \left[\frac{1}{6.55}\left(1 - \frac{1}{H}\right)\right]^2 \qquad (9)$$

(East and Sawyer, 1979). Table 1 also shows that $\overline{p^2}/\tau_M^2$ from Panton and Linebarger is nearly constant while $\overline{p^2}/\tau_w^2$ varies over an order of magnitude. This scaling on τ_M is supported by equation (3) and the structure of strong adverse pressure gradient boundary layers.

Perry and Schofield (1973) proposed universal empirical correlations for the inner and outer mean velocity profile regions of strong adverse-pressure-gradient boundary layers near separation. Their work was based upon 145 mean velocity profiles taken from Coles and Hirst (1969), including both equilibrium and non-equilibrium profiles. The data of Simpson et al. (1977; 1981 a, b, c) upstream of any flow reversal agree with these correlations. The Reynolds shearing stress profile and the maximum shearing stress τ_M (which occurs in the middle of the boundary layer) play important roles in these correlations when $\tau_M > 1.5 \tau_w$. In other words, the same large-scale turbulent structures that produce the maximum shearing stress away from the wall are the structures that influence the mean velocity profile from near the wall to the outer edge.

Perry and Schofield proposed that the outer region flow be described by

$$\frac{U_\infty - U}{U_s} = f_2\left(\frac{y}{\Delta}\right) , \qquad \Delta = 2.86 \frac{\delta^* U_\infty}{U_s} \qquad (10)$$

with

Table 1. Some pressure fluctuation results from adverse-pressure-gradient turbulent boundary layers

Authors	$Re_{\delta^*} \times 10^{-3}$	$\dfrac{U_\tau}{U_\infty}$	Π	H	$\dfrac{U_M}{U_\infty}$	$\dfrac{\delta U_\tau}{\nu}$	$\dfrac{\overline{p^2}}{\tau_W^2}$	$\dfrac{\overline{p^2}}{\tau_M^2}$	$\Phi(\omega_l)(\omega_l)^{-1}$ region	$\Phi(\omega_l)(\omega_l)^{-3}$ region	Comments
Panton & Linebarger (1974) calculations; equilibrium	9.8	0.0307	1.5	1.49	0.0504*	-	19.1	2.62	NA	NA	$\alpha = 1$
	39.1	0.0251	3	1.627	0.0589*	-	62.4	2.06	$\omega_l \approx 0.6$	$1 < \omega_l < 3$	$\alpha = 1$
	39.1	0.0251	3	1.627	0.0589*	-	130	4.29	$\omega_l \approx 0.4$	$1 < \omega_l < 3$	$\alpha = 2$
	68.3	0.0183	6	1.824	0.0690*	-	395	1.96	NA	NA	$\alpha = 1$
Bradshaw (1967) equilibrium	40.3	0.0252	2.9	1.59	0.0566	191	78	3.4	$\omega_l \approx 0.6$	$3 < \omega_l < 6$	piezoelectric transducer; X = 1.22 m
Lim (1971) equilibrium	28.4	0.0291	1.92*	1.56	0.0546*	53.8	16.8	1.52	$0.8 < \omega_l < 2$	not observed	X = 2.9 m; piezo-electric transducer X = 3.2 m; no turbulence measurements
	32.4	0.0294	1.92*	1.52	0.0519*	59.2	18.8	1.73	"	"	
Schloemer (1966) non-equilibrium	14.6	0.0296	1.84*	1.58	0.0563*	126	18.9	1.44	$0.8 < \omega_l < 1$	$\omega_l > 6$	piezoelectric
Burton (1973) non-equilibrium	NA	0.023	NA	1.76	0.059	≈ 38	92	2.12	$\omega_l \approx 0.4$	$\omega_l > 2$	X/δ^* = 14.5; pinhol microphone X/δ^* = 24.3
	38.	0.021	4.7*	2.23	0.060		131	1.97	"	"	
Hahn (1976) airfoil	48.	0.030	0.9*	1.33	0.038	274	19.6	7.5	$0.5 < \omega_l < 10$	NA	piezoelectric transducers
Brooks & Hodgson (1981) airfoil	19.	0.032	NA	1.5	0.051*	40	NA	NA	$0.5 < \omega_l < 5$	NA	piezoelectric transducers

$\omega_l = \omega\delta^*/U_\infty$; * denotes values estimated from equilibrium boundary layer equations for the laws of wall and wake or equation (9); NA denotes data not available.

$$U_s \approx 8 \sqrt{\frac{\tau_M}{\rho}} \left(\frac{\Delta}{N}\right)^{1/2} \tag{11}$$

and N being the distance from the wall to the maximum in the local shear-stress profile.

Thus using equations (3), (10) and (11) and scaling the turbulence structure on τ_M and Δ produces the result that

$$p \sim \rho U_s U_M \tag{12}$$

or that

$$p \sim \tau_M \left(\frac{\Delta}{N}\right)^{1/2} \sim \tau_M \left(\frac{\delta^* U_\infty}{N U_M}\right)^{1/3} \tag{13}$$

Table 1 shows that $\overline{p^2}/\tau_M{}^2$ values from experiments are in approximate agreement with Panton and Linebarger's calculations. It appears that $\overline{p^2}/\tau_M{}^2$ decreases with increasing H, although there are insufficient data to be sure of this and the Δ/N dependence given in equation (13). When $\tau_M/\tau_w < 1.5$, we would expect $\overline{p^2}/\tau_M{}^2$ to approach 9, which is about the zero pressure gradient value. Hahn's (1976) data support this observation. The effect of transducer size on these data is not clear since $\overline{p^2}/\tau_M{}^2$ does not consistently decrease with dU_τ/ν.

Figure 2 shows spectra corrected for transducer size, that correspond to the strong adverse pressure gradient data of Table 1 when normalized on τ_M. The data of Schloemer, Bradshaw, Burton and Lim for H < 2 and the calculations of Panton and Linebarger for $\alpha = 1$ agree within a few dB for $\omega\delta^*/U_\infty < 5$. All results seem to agree at $\omega\delta^*/U_\infty = 1$. At higher $\omega\delta^*/U_\infty$ values, Lim's data are much higher than that of the others and Panton and Linebarger's calculations appear to be higher. As shown in Table 1, the ω^{-1} region becomes narrower at
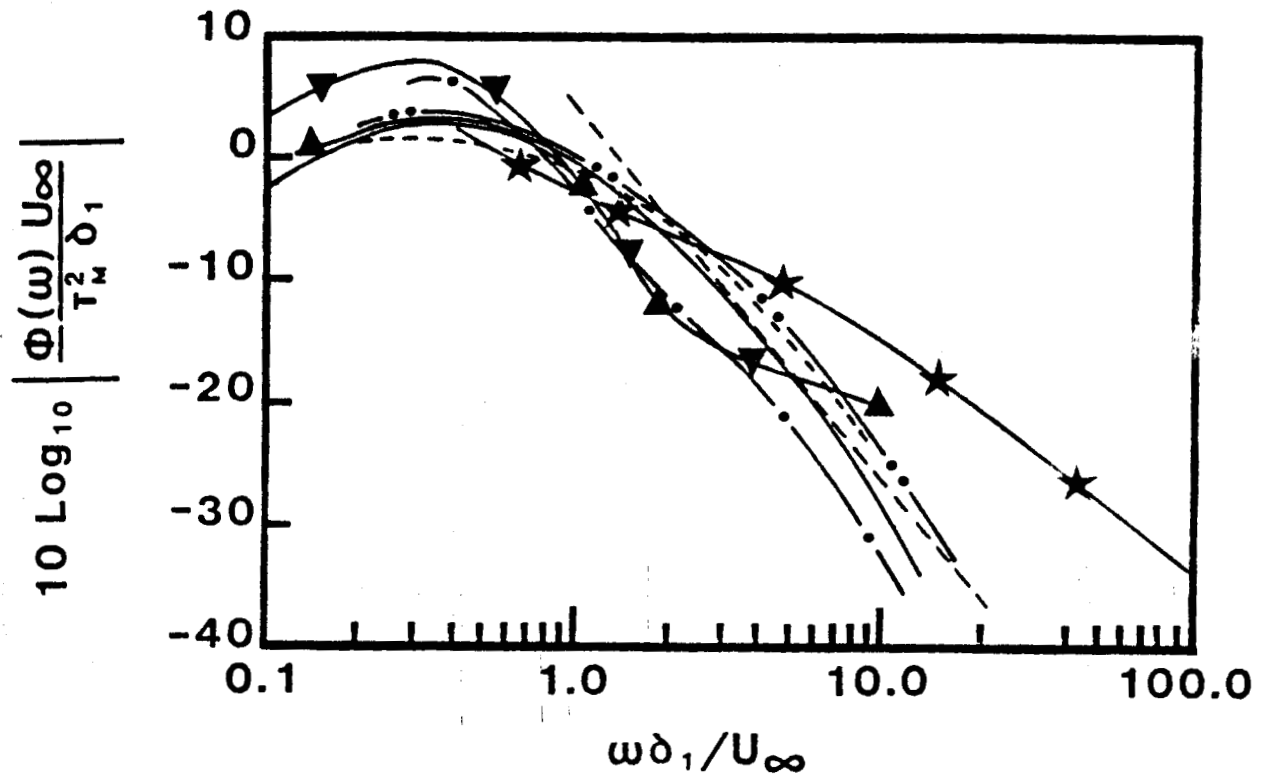
Figure 2: Spectra from some strong adverse pressure gradient
turbulent boundary layers. Straight dashed line:
ω^{-3} variation.

higher H values until it is only a point near $\omega\delta^*/U_\infty = 0.5$. A ω^{-3} region at higher frequencies is observed for the higher H values.

The $\alpha = 2$ calculations of Panton and Linebarger agree fairly well with Burton's spectral data for H = 2.23. These calculations suggest that the ratios of streamwise length scale to length scales in other directions are greater than one for strongly retarded boundary layers. The spatial correlation data of Schubauer and Klebauoff (1951) for a strongly retarded separating turbulent boundary layer indicate that the streamwise integral length scale was about 2.5 times the normal-to-wall integral length scale. The calculations of Panton and Linebarger suggest that $\overline{p^2}/\tau_M^2 \sim \alpha$. The spectrum above $\omega\delta^*/U_\infty = 1$ does not appear to be influenced by α, either in calculations or in the data. Thus, the low frequency part of the spectrum for strongly-retarded adverse pressure gradient boundary layers appears to be large because α is much greater than one.

Panton and Linebarger proposed that the convective velocity $U_c(k)$ for the overlap region or k^{-1} part of the spectrum for an attached boundary layer can be described by

$$\frac{U_c}{U_\tau} = \frac{1}{K} \ln / \frac{u_\tau}{k\nu} / + 5.0 \tag{14}$$

This expression is the same as the semi-logarithmic mean velocity profile equation, with $U_c = U$ at $y = 1/k$. They showed that this expression agrees very well with the data of Bradshaw (1967) and Wills (1970) for $6 < k\delta < 40$ or the k^{-1} part of the spectrum. This expression also fits the measured U_c/U_∞ data of Schloemer within 10% for adverse, zero, and favorable

pressure gradients in the ω^{-1} part of the spectrum. The adverse pressure gradient data of Burton, Brooks and Hodgson and Hahn for the closest sensor spacings also are described within 15% by this equation in the overlap region.

These latter sets of data, obtained using space-time correlations or cross-spectral phase information, show that the apparent U_c increases with increasing sensor spacing because the coherence of smaller scale turbulent motions at a given frequency decays more. Schloemer found that the decay of a particular frequency component with respect to distance was more rapid in an adverse gradient and slower in a favorable gradient than the decay in a zero pressure gradient. This amounts to spatial filtering of the eddies, causing the more coherent faster large-scale structures to contribute more to the apparent U_c at increasing spacings. Bradshaw (1967) pointed out that the average convection velocity at a given wavenumber k is the average over all frequencies in the (k, ω) plane. Like Wills, Bradshaw took the one-dimensional Fourier transform of frequency-filtered spatial correlations to obtain $U_{cn}(k, \omega)$. This approach produces the complete distribution of U_{cn} at all k, while spatial-filtering approaches produce large-eddy weighted averages.

The convective velocity reaches a peak value at a frequency near the lower end of the overlap part of the spectrum. Bradshaw's data show this peak near $\omega\delta^*/U_\infty = 0.5$, while Brooks and Hodgson show a peak near $\omega\delta^*/U_\infty = 3.0$. Brooks and Hodgson, Wills and Bradshaw show that U_c decreases below this peak. Schloemer and Burton do not have data for this low frequency range while Hahn's results show numerous U_{cn} maxima and

minima. Panton and Linebarger suggested an approximate wake function expression for this low frequency range.

In addition to these types of data, some measurements in zero pressure gradient flows have been obtained that lead to a better understanding of the structural interrelationships between the velocity and surface pressure fluctuations. Thomas and Bull (1983) conditionally-sampled wall-pressure fluctuations on the basis of the high-frequency activity of the pressure fluctuations themselves, the high-frequency activity of the streamwise velocity fluctuations in the vicinity of the wall, and the excursions in velocity in the vicinity of the wall. This led to the identification of a characteristic wall-pressure fluctuation pattern which is associated with the burst-sweep cycle of events in the wall region. The pattern has the form of an overpressure over a streamwise extent of about $1 \cdot 5$-$2 \cdot 0\delta^*$ with a region of underpressure and a pressure minimum to either side of it, the distance between pressure minima being about $3 \cdot 0$-$3 \cdot 5\delta^*$. This pattern is convected at a velocity $0 \cdot 67$ times the freestream velocity. Its phase relationship with velocity fluctuations close to the wall and the wall shear-stress fluctuations during the burst-sweep cycle were established. It appears to be produced by the inclined shear layer which forms the upstream surface of the large organized structures in the layer, and calculated pressure patterns support this conclusion.

The phase relationships indicate that fluid involved in the bursting process is subjected to a favorable streamwise pressure gradient by the characteristic wall-pressure pattern at the time that the lift-up of low-speed streaks in the wall region begins. In addition, order-of-magnitude estimates suggest that the adverse pressure gradients associated

with the characteristic pressure pattern, even if their phasing with streak lift-up were appropriate, would be insufficient to initiate the lift-up. It was concluded that the streamwise pressure gradients associated with the pressure patterns do not play an active role in the dynamics of the wall flow and are not the direct cause of the bursting process. Unfortunately, no studies of this type have been performed in the presence of strong adverse pressure gradients or separation.

Mabey (1972) presented a rough correlation of rms pressure fluctuations and spectra for step-induced separation and reattachment flows. The length of the detached flow zone S is a good normalizing length that causes the shapes of the plots to be similar. In p'/q vs. X/S plots, p' increases rapidly after detachment, reaching an order of magnitude greater maximum just upstream of reattachment. At this maximum, p'/q_∞ varied from 0.04 to 0.1, depending on the type of detached flow. In $nF(n)$ vs. nS/U_∞ spectral plots, the peak frequency is located just below a nS/U_∞ of one. Since no data for the Reynolds shear stress $-\rho\overline{uv}$ profiles are available, it is not possible to correlate further these data.

Kiya et al. (1982) showed similar results for a forward-facing step flow: p'/q_∞ reached a maximum of 0.14 at $X/L = 1$; $nF(n)$ reaches a maximum at $nS/U_\infty \approx 0.7$ and decays proportional to n^{-2} at higher frequencies. Near reattachment, $p'/\tau_M \approx 10$, which is an order of magnitude greater than the values given in Table 1 for attached flows.

III. DESCRIPTION OF THE WIND TUNNEL AND THE TEST FLOW

A. Wind Tunnel

This facility is same one used in earlier work on steady and un-
steady separating turbulent boundary layers (Simpson et al., 1981 a, b,
c, 1983 a, b). The mainstream flow of the blown open-circuit wind
tunnel is introduced into the test section after first passing through a
filter, blower, flow dampers, a section of honeycomb to remove the mean
swirl of the flow, seven screens to remove much of the turbulence in-
tensity, and finally through a two-dimensional 4:1 contraction-ratio nozzle
to further reduce the longitudinal turbulence intensity while accelerating
the flow to test speed.

Figure 3 is a side-view schematic of the 8 m long, 0·91 m wide test
section of the wind tunnel. The upper wall is adjustable such that the
free-stream velocity or pressure gradient can be adjusted. The sidewalls
are made of float plate glass to prevent laser signal dispersion, while
the upper wall is made of Plexiglas.

The active boundary-layer control system, which is described by
Simpson, Chew and Shivaprasad (1980), was installed on the non-test
walls of the test section to inhibit undesirable flow three-dimension-
ality and to prevent separation. Because the static pressure in the
test section is time-varying in unsteady experiments, no passive
boundary-layer control can be used that depends on a steady test section
pressure higher than the pressure outside the tunnel. Highly two-
dimensional wall jets of high-velocity air are introduced at the beginning
of each of the eight-feet long sections. At the latter two streamwise
locations the oncoming boundary layer is partially removed by a highly

Figure 3: Sideview schematic diagram of the test section with the steady
free-stream separating turbulent boundary layer (Simpson et al.
1981a) on the bottom wall. The major division on the scales are
10 in. Note the baffle plate upstream from the blunt leading
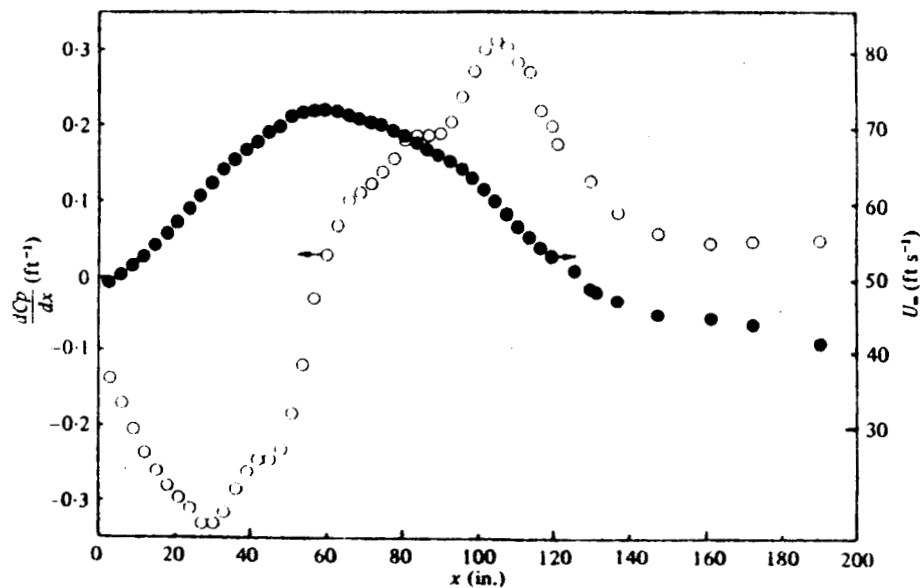edge on the bottom test wall and side- and upper-wall jet
boundary-layer controls.

Figure 4: Free-stream velocity and pressure gradient distribution along
the tunnel center-line.
$C_p = 2(P-P_i)/\rho U_{\infty i} = 1-(U_\infty - U_{\infty i})^2$, $U_{\infty i} = 49 \cdot 4$ ft s^{-1}.

two-dimensional suction system.

The inviscid core flow is uniform within 0·05% in the spanwise direction and within 1% in the vertical direction. The test-wall boundary layer is tripped by the blunt leading edge of the plywood floor, the height of the step from the wind-tunnel contraction to the test wall being 0·63 cm. Smoke can be introduced uniformly into the boundary layer just upstream of this trip for use with the laser anemometer.

B. Summary of the Nature of This Steady Free-stream Separating Turbulent Boundary Layer

All data presented here in the earlier works on this flow were obtained at atmospheric pressure and $25 \pm \frac{1}{4}$ °C conditions. Figure 4 shows the free-stream velocity distributions obtained along the tunnel center-line using the single-wire probe. This distribution was repeatable within 2·9% over the duration of these experiments, which is only a little greater than the uncertainty in measuring the mean velocity with a hot-wire anemometer ($\pm$ 2·4%). Figure 4 also shows the non-dimensional pressure gradient dC_p/dx along the centerline of the test wall. Hence $C_p \equiv 2(P-P_i)/\rho U_{\infty i}^2 = 1 - (U_\infty/U_{\infty i})^2$, where i denotes the free-stream entrance conditions at a distance x of 7.6 cm. A five-point local least-squares curve fit of C_p data was used at each streamwise location to determine this derivative. Just downstream of the location of the second wall-jet boundary-layer control unit (2.5 m), the slope of the static pressure gradient changes sign. Near 3.7 m the pressure gradient drops to an approximately constant value downstream. As discussed

in more detail by Simpson et al. (1981 a), the mean boundary-layer flow appears to be two-dimensional in the center third of the channel width upstream of 4.3 m.

For steady free-stream mean-two-dimensional separating turbulent boundary layers, a set of quantitative definitions on the detachment state near the wall has been proposed (Simpson 1981): incipient detachment (ID) occurs with instantaneous backflow 1% of the time; intermittent transitory detachment (ITD) occurs with instantaneous backflow 20% of the time; transitory detachment (TD) occurs with instantaneous backflow 50% of the time; and detachment (D) occurs where the time-averaged wall shearing stress $\overline{\tau}_w = 0$. Thus the fraction of time with forward flow γ_{pu} is a descriptive parameter for identifying these stages and should be documented in all separated-flow experiments.

Figure 3 shows a qualitative sketch of the steady free-stream bottom-wall turbulent shear flow studied with a laser anemometer at SMU and the locations of ID, ITD and D when determined 1 mm from the wall. The mean flow upstream of ID obeys the 'law of the wall' and the 'law of the wake' as long as the maximum shearing stress $-\rho\overline{uv}_{max}$ is less than $1 \cdot 5\tau_w$. The qualitative turbulence structure is not markedly different from the zero-pressure-gradient case. The 'bursting' frequency n of the most-energetic eddies near the wall is correlated by $U_\infty/n\delta = 10$, where U_∞ is the mean velocity outside the boundary layer and δ is the boundary-layer thickness.

When $- \rho\overline{uv}_{max} > 1 \cdot 5\tau_w$, the Perry and Schofield (1973) mean-velocity-profile correlation and the law of the wall apply upstream of

ITD. Up to one-third of the turbulence energy production in the outer region is due to normal-stress effects, which modify the relations between dissipation rate, turbulence energy and turbulent shearing stress that are observed farther upstream. The spanwise integral lengthscale of the turbulence increases with δ^2, and the bursting frequency n continues to be about equal to $U_\infty/10\delta$. Pressure-gradient relaxation begins near ITD and continues until D.

Downstream of detachment, the mean backflow profile scales on the maximum negative mean velocity U_N and its distance N' from the wall. A u^+ vs. y^+ law of the wall is not consistent with this result since U_N and N increase with streamwise distance while $\nu/(\tau/\rho)_w^{1/2}$ varies with $(\tau/\rho)_w^{1/2}$. High turbulence levels exist in the backflow, with u- and v-fluctuations of the same order as $|U|$. $-\overline{uv}/u'v'$ becomes lower with increasing backflow, and is about 25% lower in the outer region than for the upstream attached flow. Mixing-length and eddy-viscosity models are adequate upstream of detachment and in the outer region, but are physically meaningless in the backflow. γ_{pu} never reaches zero, indicating that there is no location with backflow all of the time. Normal and shear stresses turbulence energy production in the outer region supply turbulence energy to the backflow by turbulence diffusion where it is dissipated. Negligible turbulence-energy production occurs in the backflow.

This turbulence-energy diffusion and the small mean backflow are supplied intermittently by large-scale structures as they pass through the detached flow as suggested by Figure 3. The backflow does not come from far downstream. The frequency of passage n of these large-scale

structures also varies as U_∞/δ and is about an order of magnitude smaller than the frequency far upstream of detachment. Reynolds shearing stresses in the backflow must be modelled by relating them to the turbulence structure and not to local mean-velocity gradients. The mean-velocity profiles in the backflow are a result of time-averaging of the large fluctuations and are not related to the cause of the turbulence.

IV. INSTRUMENTATION AND EXPERIMENTAL TECHNIQUES

A. Hot-wire Anemometers and Probes

Miller-type (1976) integrated circuit hot-wire anemometers and linearizers, as modified by Simpson, Heizer, and Nasburg (1979) were used. A standard TSI model 1244-T1.5 dual hot-wire probe was used for the stream-wise velocity fluctuation wavespeed and spectral measurements with a 5mm spacing between the parallel sensors. The frequency response for each sensor was flat up to 7.5 KHz for an overheat ratio of 1.7. The upstream sensor was used to obtain all spectral data.

Calibrations were made in a TSI Model 1127 calibrator and in the core flow of the throat of the wind tunnel test section at various speeds. There was no detectable drift of the anemometer, although the function-module-type linearizers had a small amount of d.c. drift. Each linearized calibration had a low level of dispersion from a straight line, with the product moment correlation coefficient in excess of 0.9999.

B. Microphones and Calibrations

Two Sennheiser Model MKH-110 Instrumentation Microphones were each mounted in identical plexiglas housings with pinholes for use in these

measurements. According to the manufacturer's specifications, these low frequency RF condensor microphones have a nominal sensitivity of 20 mv/Pa, nearly flat frequency response ($\pm$ 3dB) between 1 Hz and 6 KHz, an overload level of 120 dB SPL, and signal-to-noise ratio of 63 dB $\pm$ 3dB. The frequency response peaks at about 10 KHz and drops below the low frequency level of 16 KHz. Since the microphone can only be used with equal static pressures on both sides of the diaphragm, the back of the pressure sensititive element was sealed from the solid-state electronics portion. The sliding fit between the microphone and the plexiglas housing acted as a low-pass filter and permitted the volume behind the diaphragm to reach the test static pressure through vent holes on the side of the microphone.

The 2.21 cm diameter cylindrical plexiglas housings each had 0.074 cm diameter by 0.025 cm long pinholes in the center of the flat end. The 1.55 cm diameter end of a microphone fits snugly against the housing end, with the 1.35 cm diameter diaphragm 0.10 cm away from the pinhole.

Each microphone and plexiglas housing combination was calibrated with a Genrad Model 1956 Sound-Level Calibrator between 125 Hz and 4 KHz and 74 to 114 dB SPL. A calibrator consisting of a sealed volume with an oscillating piston was built and used for calibration between 0.5 Hz and 30 Hz. Using the perfect gas law the adiabatic process equations, the pressure oscillation in the sealed volume could be calculated at each test frequency from the volume oscillation produced by the piston. At low frequencies the measured sensitivity was approximately 22 mv/Pa. The following equation approximately describes the frequency response of

these microphones in their housings

$$\frac{P_{rms}}{P_{rms\ i}} = (1 - 0.437871\ f^2 - 0.0800\ f^4 + 0.0493292\ f^6)^{-1/2}$$

where the frequency f is given in KHz. This equation indicates that
the microphone sensitivity is reduced above 2 KHz because of the housing.

For the coherence and celerity measurements when the two microphones
are close together, two housings were joined adjacently. Several above-
mentioned pinholes were located on each housing end, permitting sensing
hole spacings of 1.40 to 3.02 cm. Pinholes not in use were covered by
thin cellophane tape.

C. Pressure Fluctuation Measurement Techniques

After initial use of these microphones, it was apparent that minute
wind tunnel vibrations and acoustic disturbances make large contributions
to the microphone signals. To eliminate the vibration effects, the
microphones and housings were supported directly from the concrete floor-
ing, with no direct firm contact with the adjacent test wall. Strips of
0.05mm thick celephane tape were used to make the test surface flat and
continuous between the 3.5cm diameter holes in the test wall and the
plexiglas housings.

In this wind tunnel, there are streamwise acoustic disturbances that
propagate downstream from the blower-muffler-plenum-honeycomb-screen
sections into the contraction. The contraction and test section act as
wave guides for these disturbances, so that at any streamwise location
the streamwise acoustic waves are the same across the test section at any
instant in time. The turbulent-flow-produced spectrum is the same across

the test section because the mean flow and mean square turbulence struc-
ture are two-dimensional across the center of the flow (Simpson et al.,
1980). The acoustic and turbulent signals are uncorrelated, since we
can see from equations (2) and (3) that the turbulence-produced signal
is due to the locally-produced velocity field. These observations
permit us to use two microphones to decompose the surface pressure
fluctuation signals into the propagated acoustic part and the turbulent-
flow-generated portion.

The two microphones and housings are spaced far apart spanwise
across the test section so that the turbulent signals are uncorrelated.
The minimum distance between sensors to produce a zero cross-correlation
is about 1/2 δ, where δ is the shear layer thickness (Simpson et al.,
1977). Physically this means that individual large-scaled motions are
no more than about δ in spanwise extent and are unrelated to one another.
In practice, for spectral measurements, ΔZ was 15 cm far upstream of
detachment and 30 cm in the detached zone.

At any spectral frequency n, the time-dependent signals detected by
these two microphones can be written as

$$p_{1n} = p_{1An} + p_{1Tn} \qquad\qquad (15\ a)$$

$$p_{2n} = p_{2An} + p_{2Tn} \qquad\qquad (15\ b)$$

where the subscripts A and T denote the acoustic and turbulent portions.
If we subtract p_{2n} from p_{1n} and obtain the mean square value of the
result, then

$$\overline{p_{1Tn}^2} = \frac{\overline{(p_{1n} - p_{2n})^2}}{2} \qquad\qquad (16)$$

is the turbulent spectral contribution at frequency n because

$$\overline{p_{1Tn}^2} = \overline{p_{2Tn}^2} \qquad \text{(mean 2-D flow)} \qquad (17\ a)$$

$$\overline{p_{1An}p_{1Tn}} = \overline{p_{2An}p_{2Tn}} = \overline{p_{1An}p_{2Tn}} = \overline{p_{2An}p_{1Tn}} = 0 \qquad (17\ b)$$

(uncorrelated acoustic and turbulent contributions)

$$\overline{p_{1Tn}p_{2Tn}} = 0 \qquad \text{(uncorrelated turbulent contributions)} \qquad (17\ c)$$

$$p_{1An} = p_{2An} \qquad \text{(same acoustic signals)} \qquad (17\ d)$$

Under these conditions the acoustic contribution at frequency n is

given by

$$\overline{p_{1An}^2} = \frac{\overline{(p_{1n} + p_{2n})^2}}{4} - \frac{\overline{p_{1Tn}^2}}{2} \qquad (18)$$

The two microphones are located equi-distant about the tunnel

centerline. Thus, equation (16) provides the proper turbulent spectrum

for frequencies below c/w, where c is the speed of sound and w is the

contraction and test section width (370 Hz). In other words, longitudinal,

vertical and spanwise acoustic contributions that are the same at the

two microphones are eliminated. However, spanwise acoustic contributions

near frequency c/w and higher harmonics are added because of the anti-

symmetry of that mode. For those frequencies the turbulent contribution

must be obtained by

$$p_{1Tn}^2 = \frac{\overline{(p_{1n} + p_{2n})^2}}{2} \qquad (19)$$

An experimental uncertainty analysis shows a negligible uncertainty in

the resulting turbulent spectrum obtained in this manner when the sensi-

tivities of the two microphones are matched, as discussed in section

IV.D below.

To determine the convective wave speed of the turbulent contributions, the two microphones were spaced a small distance ΔX apart in the streamwise direction. The wave speed or celerity at frequency n is given by

$$U_{cn} = \frac{2\pi n \Delta X}{\phi_n} \tag{20}$$

where

$$\tan \phi_n = I_n/R_n \quad , \tag{21}$$

$$\gamma^2(\Delta X, n) = R_n^2 + I_n^2 \tag{22}$$

Because the acoustic contributions at two different streamwise locations are coherent but time delayed, they can be accounted for using the measured acoustic spectra. In practice these contributions were found to be a very small part of γ for frequencies where the coherence γ^2 produces meaningful and relatively certain results (Stegan and Van Atta, 1970).

D. Signal Processing

For the pressure spectra and celerity data, the signals from each of the microphones were input to a TSI Model 1015C Correlator where the effective volts/Pa sensitivities were equalized very closely with slightly

26

different amplification ratios. Thus, with closely equal effective sensitivities, it is possible to use the sum or difference of these signals to determine pressure spectral and celerity information, as discussed in Section IV.C above. Velocity spectra and celerities were obtained in the same manner by equalizing the effective volts/mps sensitivities of the two hot-wire anemometers.

The sum or difference of these two instantaneous signals was input to a single-channel Princeton Applied Research (PAR) Model 4512 Fast-Fourier-Transform Spectrum Analyzer. The frequency resolution is 1/512 of the selectable frequency range of this 512 bin digital unit. Data records were at least 2 minutes long, which was experimentally verified to be sufficiently long for closely repeatable spectral results. A CRT display with a cursor permitted on-line viewing of spectral data.

The logarithm of the content of each bin of a spectrum was transferred from the PAR to a HP 9825T digital computer for storage on tape and further processing. Use of the logarithms of the data preserved a 1 bit uncertainty of the spectral results for the final processing. Mean square fluctuation values were computed by summing the square of the anti-logarithm values for each bin, taking into account the proper transfer function and calibration values.

V. EXPERIMENTAL RESULTS

A. Streamwise Velocity Fluctuation Spectra

Figures 5-12 show spectra for the streamwise velocity fluctuations upstream of detachment in the region of strong adverse pressure gradients. Simpson et al. (1980) report mean square velocity fluctuations for this
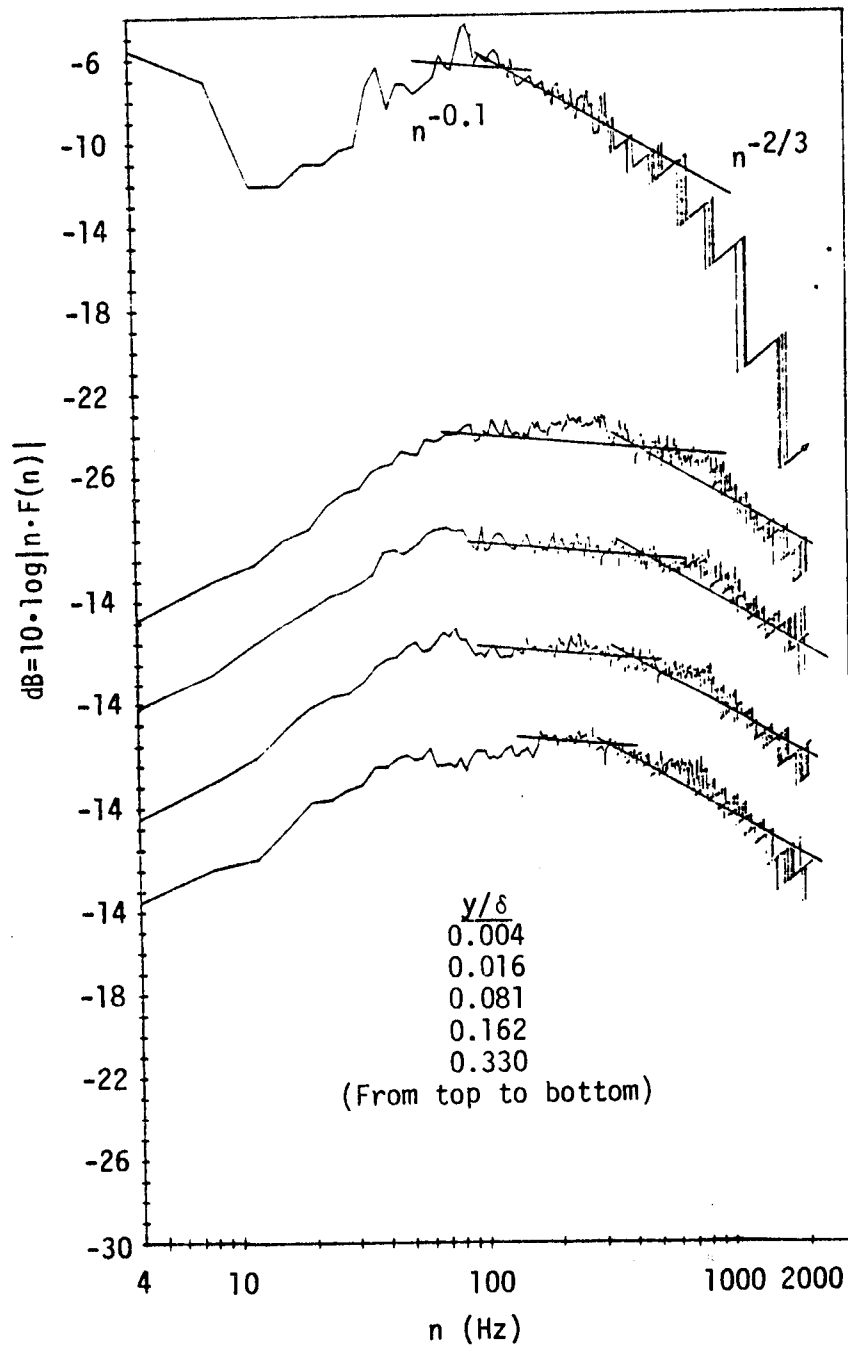
Figure 5: Velocity spectra for the downstream x location of 1.886 m. (The parameter $2\pi\delta^*/U_\infty=0.0011$ sec., also note the displaced ordinates)
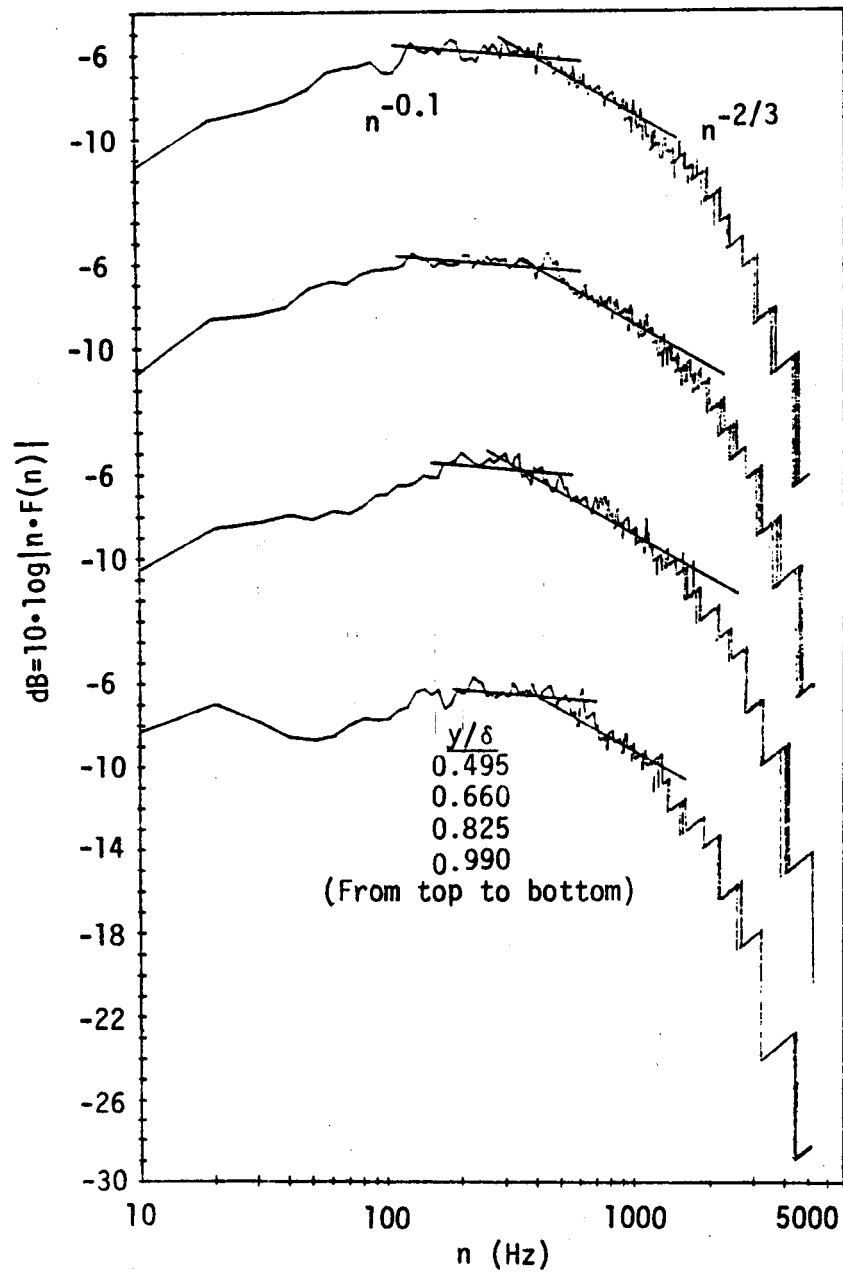
Figure 6: Velocity spectra for the downstream x location of 1.886 m. (The parameter $2\pi\delta^*/U_\infty = 0.0011$ sec., also note the displaced ordinates)
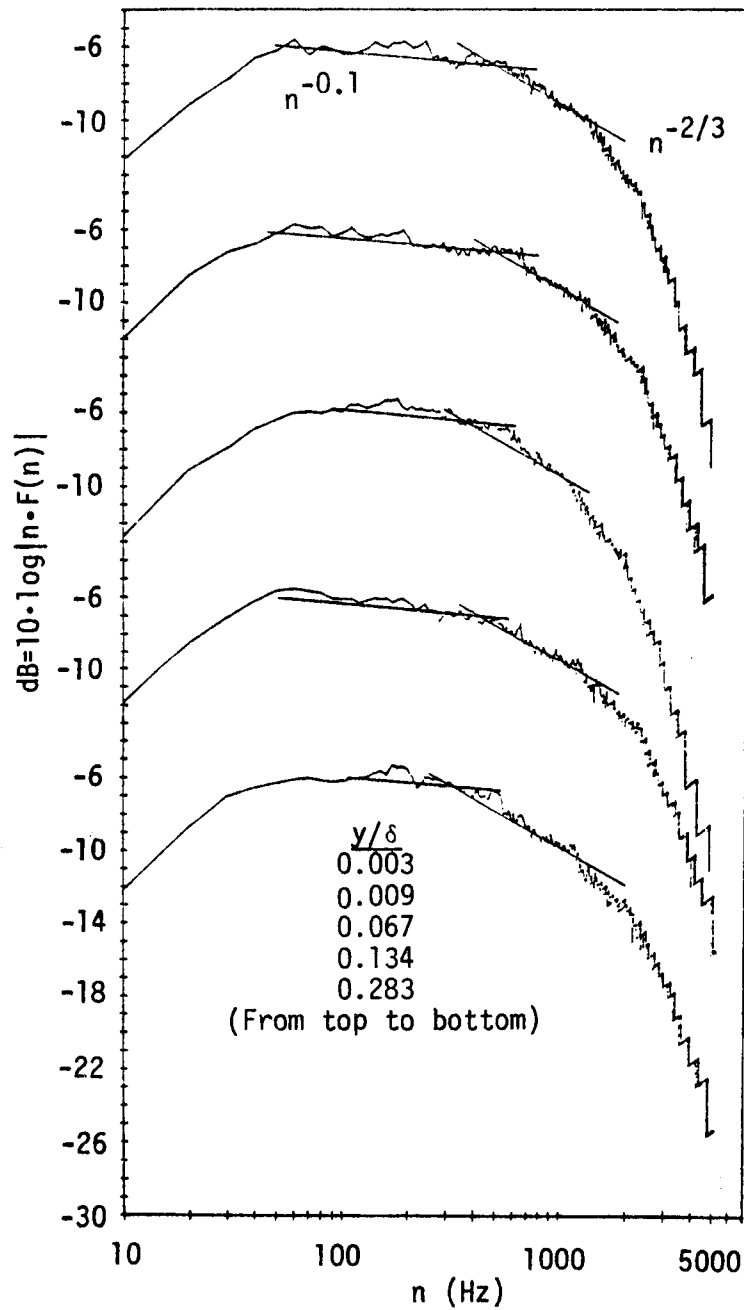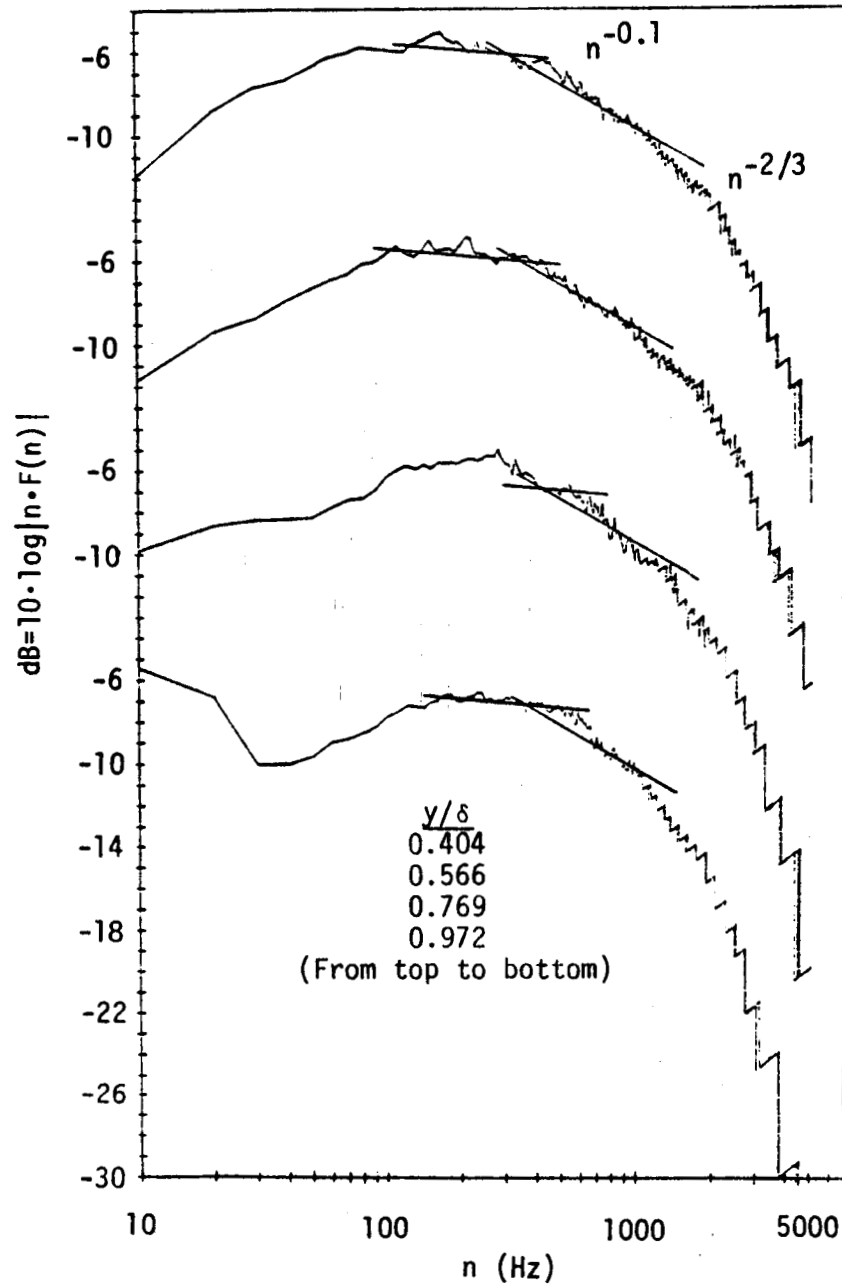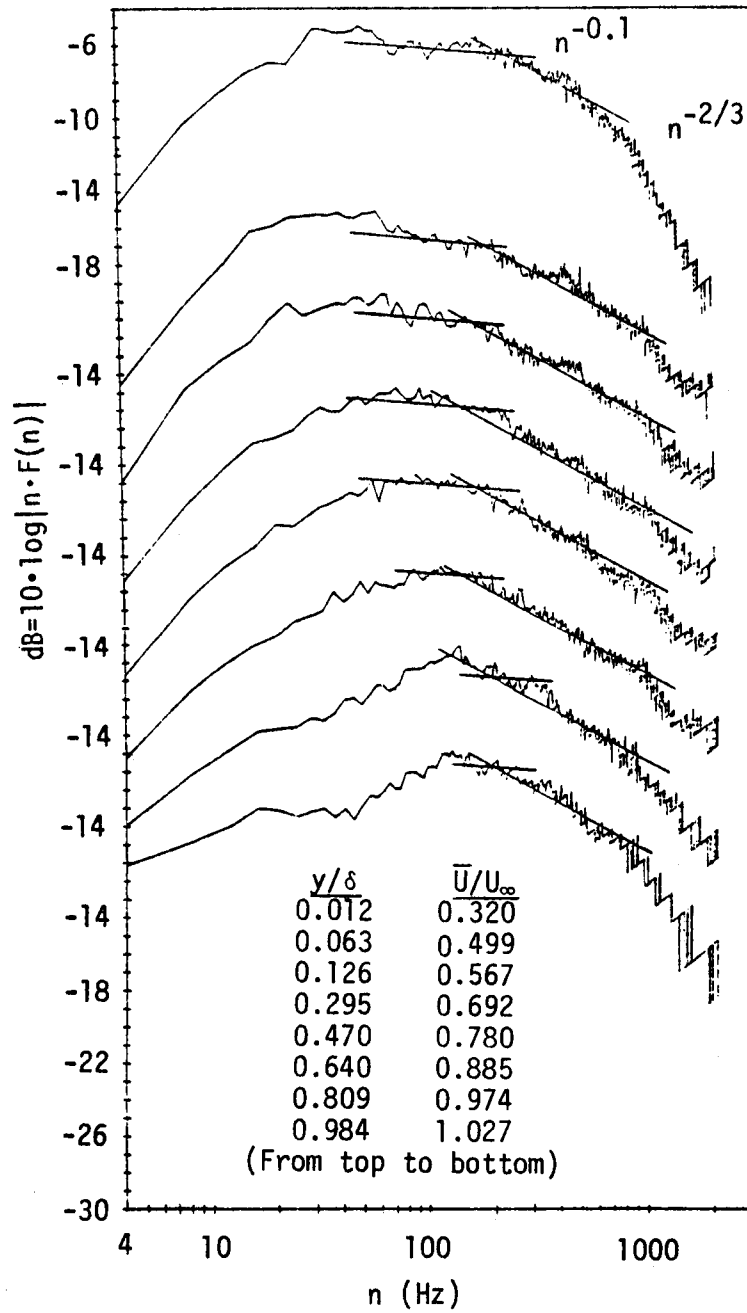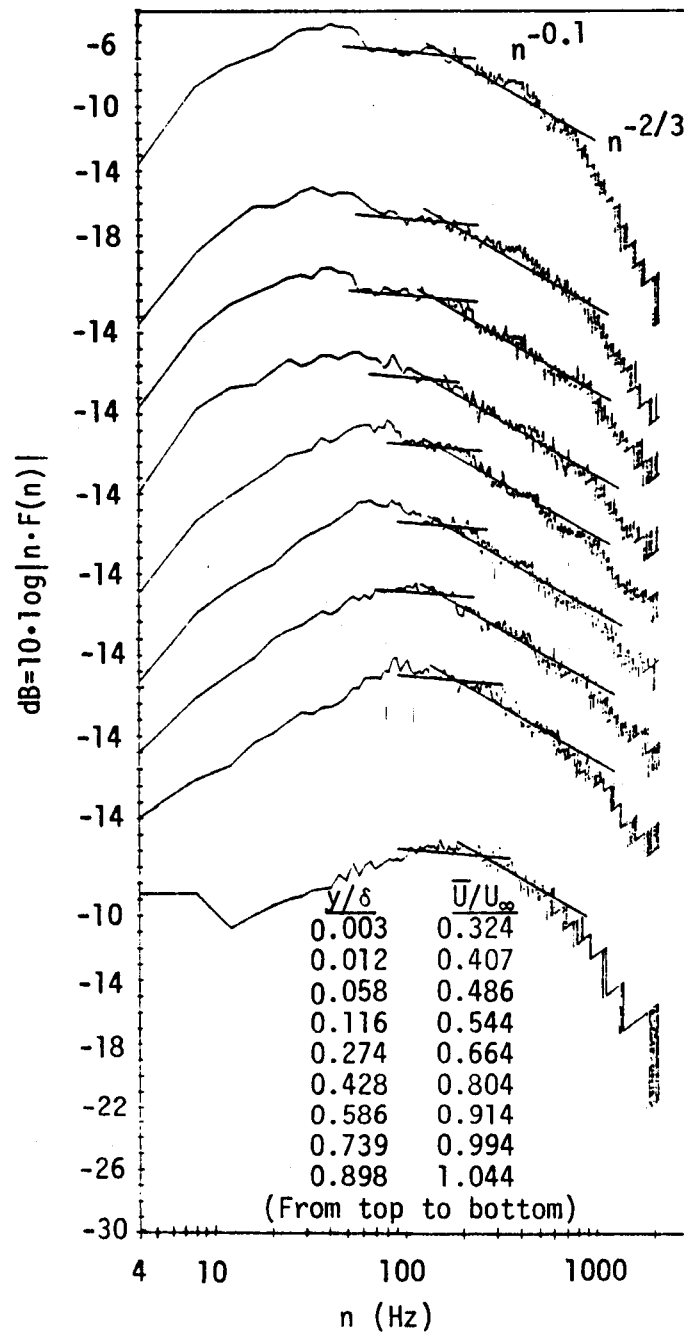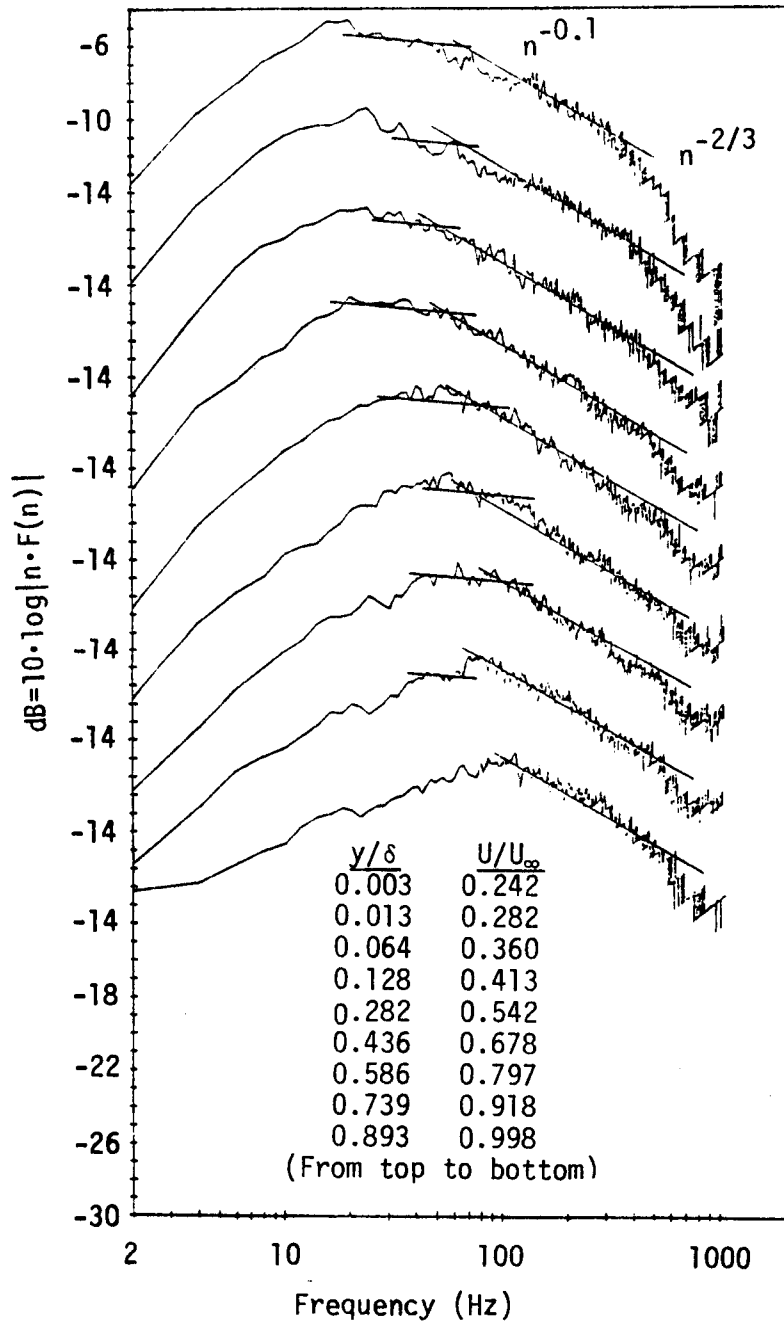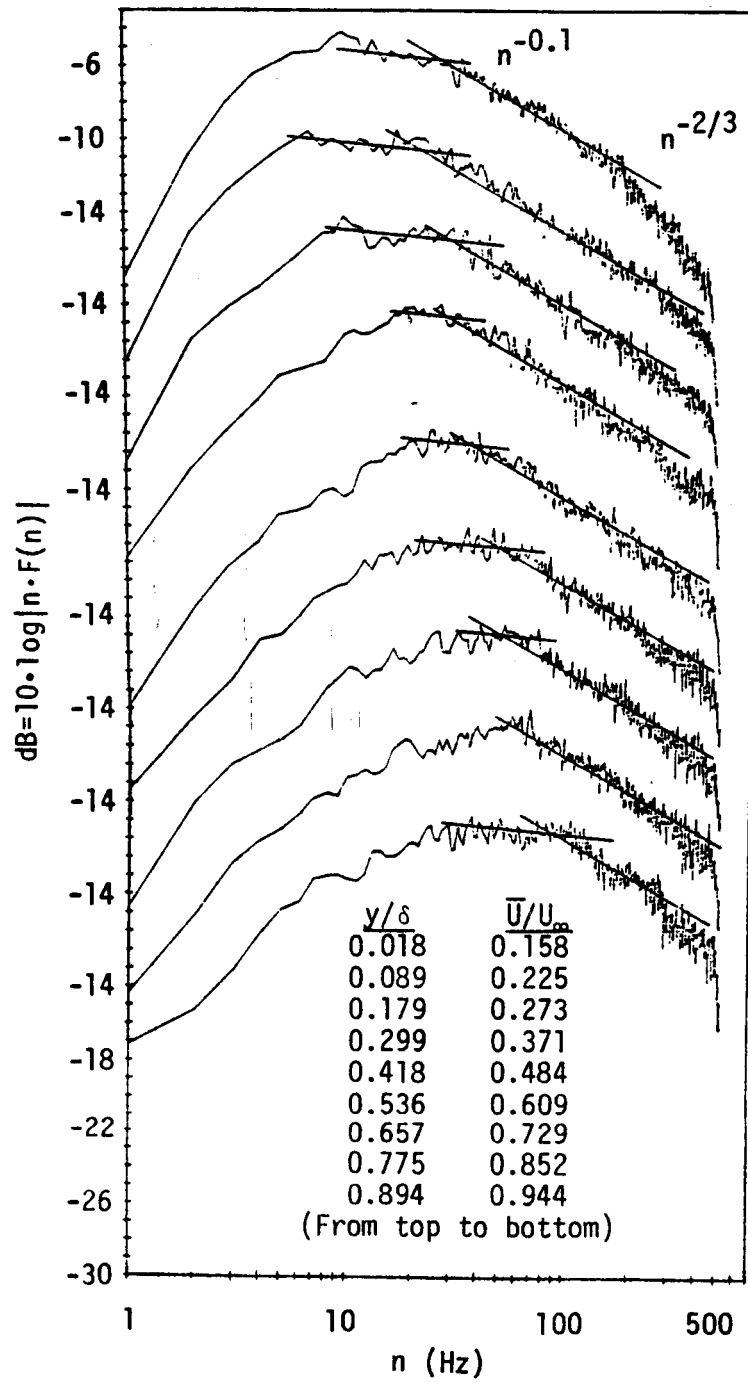
Figure 7: Velocity spectra for the downstream x location of 2.222 m.
(The parameter $2\pi\delta^*/U_\infty=0.0017$ sec., also note the displaced ordinates)

31

Figure 8: Velocity spectra for the downstream x location of 2.222 m. (The parameter $2\pi\delta^*/U_\infty=0.0017$ sec., also note the displaced ordinates)

Figure 9: Velocity spectra for the downstream x location of 2.7 m. (The parameter $2\pi\delta^*/U_\infty=0.0041$ sec., also note the displaced ordinates)

33

Figure 10: Velocity spectra for the downstream x location of 2.854 m. (The parameter $2\pi\delta^*/U_\infty=0.0059$ sec., also note the displaced ordinates)

Figure 11: Velocity spectra for the downstream x location of 3.009 m. (The parameter $2\pi\delta^*/U_\infty=0.0089$ sec., also note the displaced ordinates)

Figure 12: Velocity spectra for the downstream x location of 3.228 m.
(The parameter $2\pi\delta^*/U_\infty=0.0174$ sec., also note the displaced ordinates)

flow. Here we present the spectra in the form of $10 \log_{10}/nF(n)/$ vs. $\log_{10}/n/$ since

$$\int_0^\infty [nF(n)] \, d(\ln/n/) = 1 \tag{23}$$

by definition of $F(n)$. Thus the peaks or plateaus of $nF(n)$ plots show the most energetic spectral frequencies.

Near the wall in the semi-logarithmic mean velocity profile region, $nF(n)$ is nearly constant $(n^{-0.1})$ over a relatively wide frequency range. A definite $F(n) \sim n^{-5/3}$ inertial subrange spectral region is seen at higher frequencies as expected. As detachment is approached, smaller $F(n) \sim n^{-1}$ regions are observed. No specific frequencies with large contributions are observed, so the wind tunnel acoustic fluctuations are definitely not interacting with the turbulence to produce velocity spectrum contributions. At progressive downstream locations, the frequency range for the weak contributions decreases, as Simpson et al. (1977) observed for a slightly different separating flow. Near and downstream detachment, the inertial subrange begins at progressively higher frequencies at higher y/δ for a given X, as observed in Figures 12-16. The $U_\infty/n\delta$ values for the peak frequency of each $nF(n)$ distribution in the middle and outer boundary layer regions are about 10 ± 3, as observed by Simpson et al.(1981 b) upstream and downstream of detachment from laser anemometer data.

B. **Streamwise Velocity Fluctuation Celerities**

Figures 17 and 18 show some velocity fluctuation celerity results calculated using equations (20-22) for the data obtained from the parallel hot-wires that are a distance $\Delta X = 5$ mm apart. The wave celerity U_{cn} is a function of spatial position and frequency, but not the streamwise spacing between the two sensors (Favre et al., 1967). As observed by
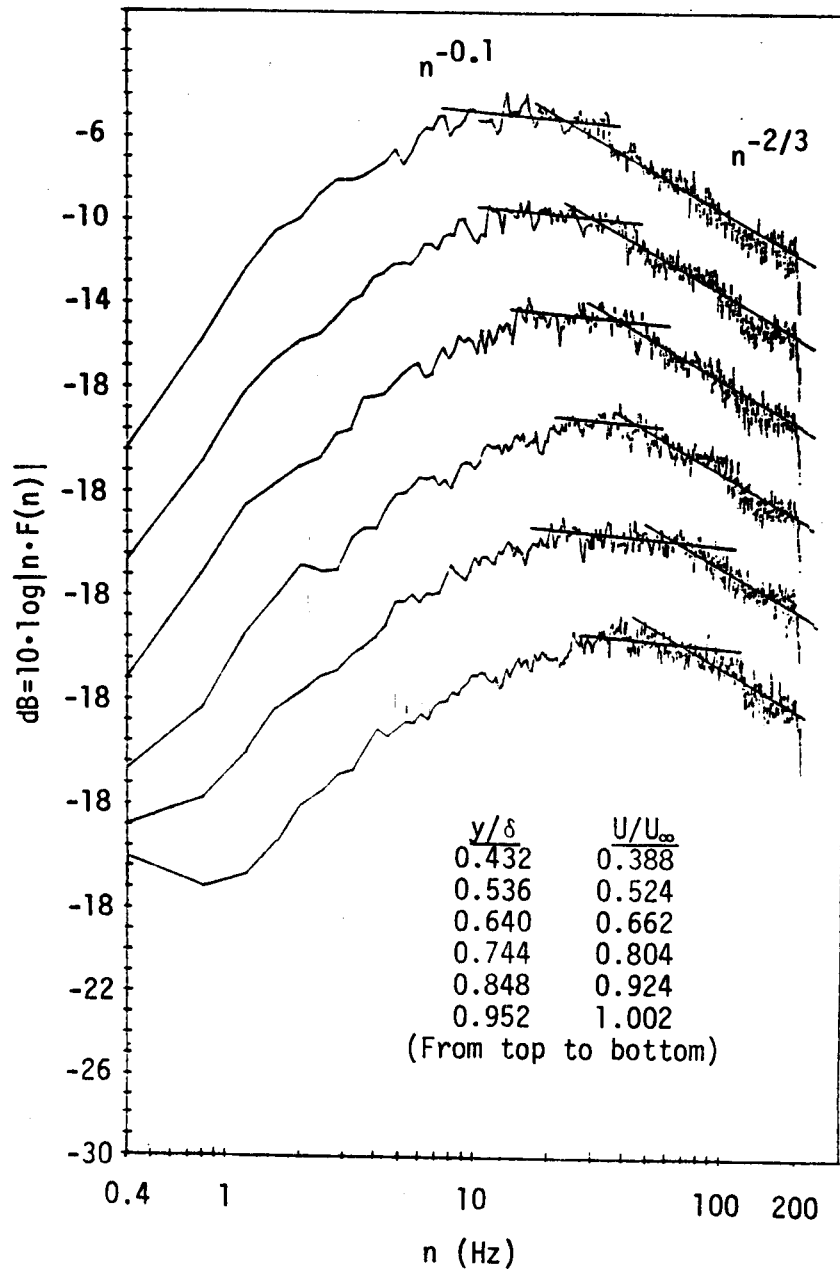
37

Figure 13: Velocity spectra for the downstream x location of 3.527 m. (The parameter $2\pi\delta^*/U_\infty=0.0351$ sec., also note the displaced ordinates)

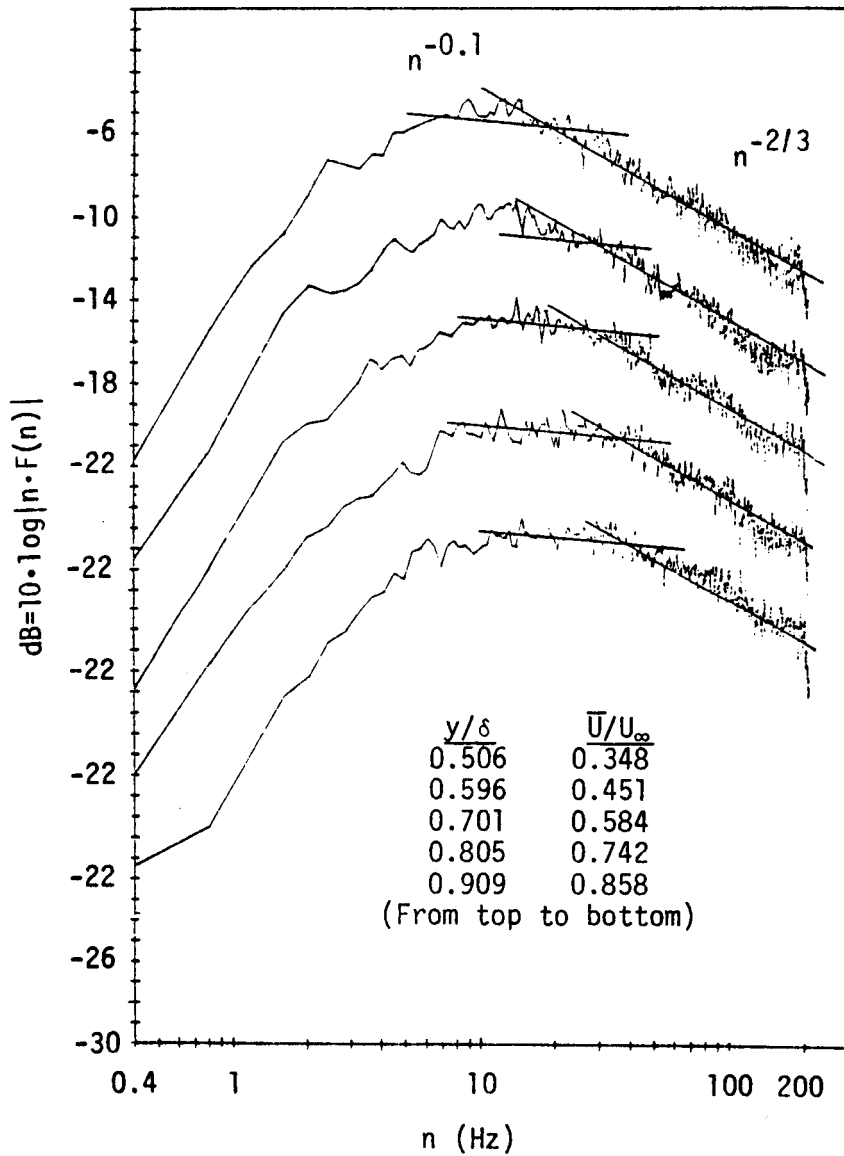Figure 14: Velocity spectra for the downstream x location of 3.679 m. (The parameter $2\pi\delta^*/U_\infty=0.0462$ sec., also note the displaced ordinates)
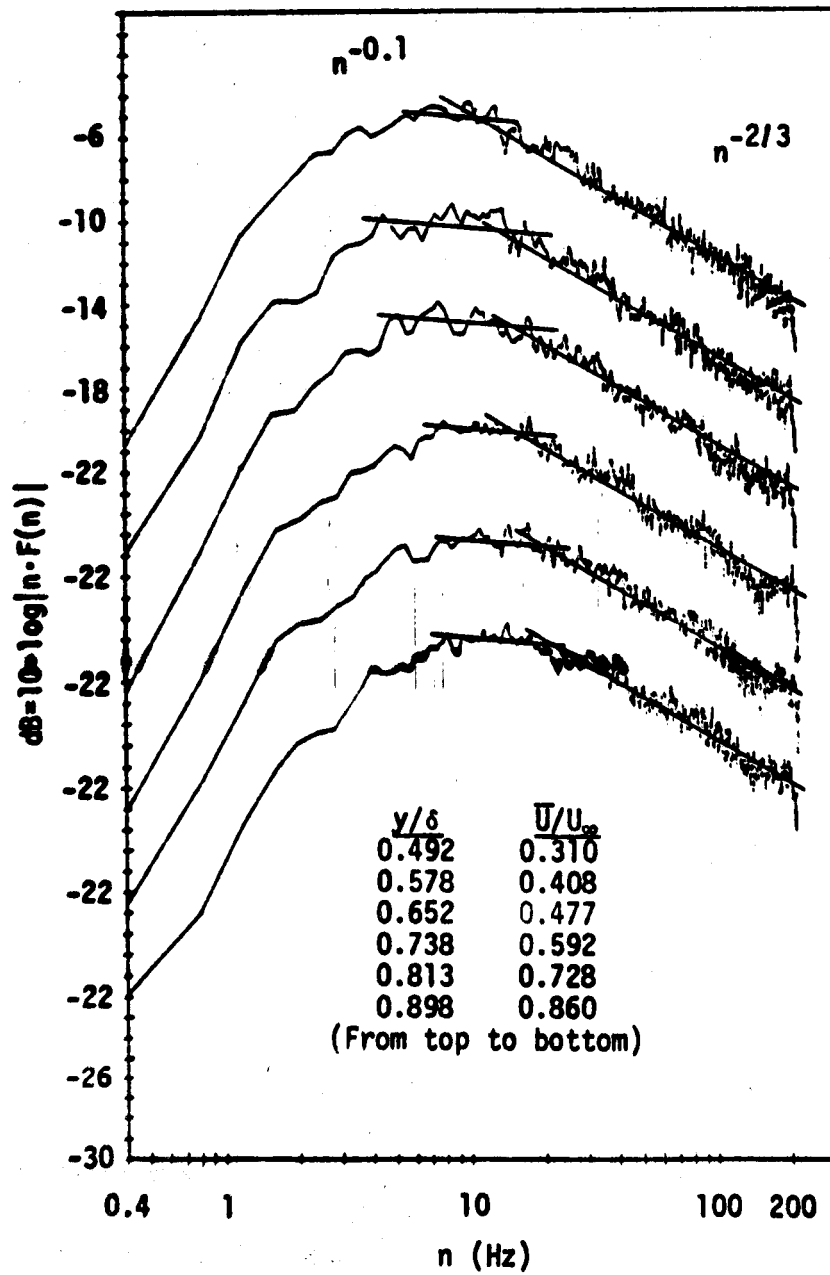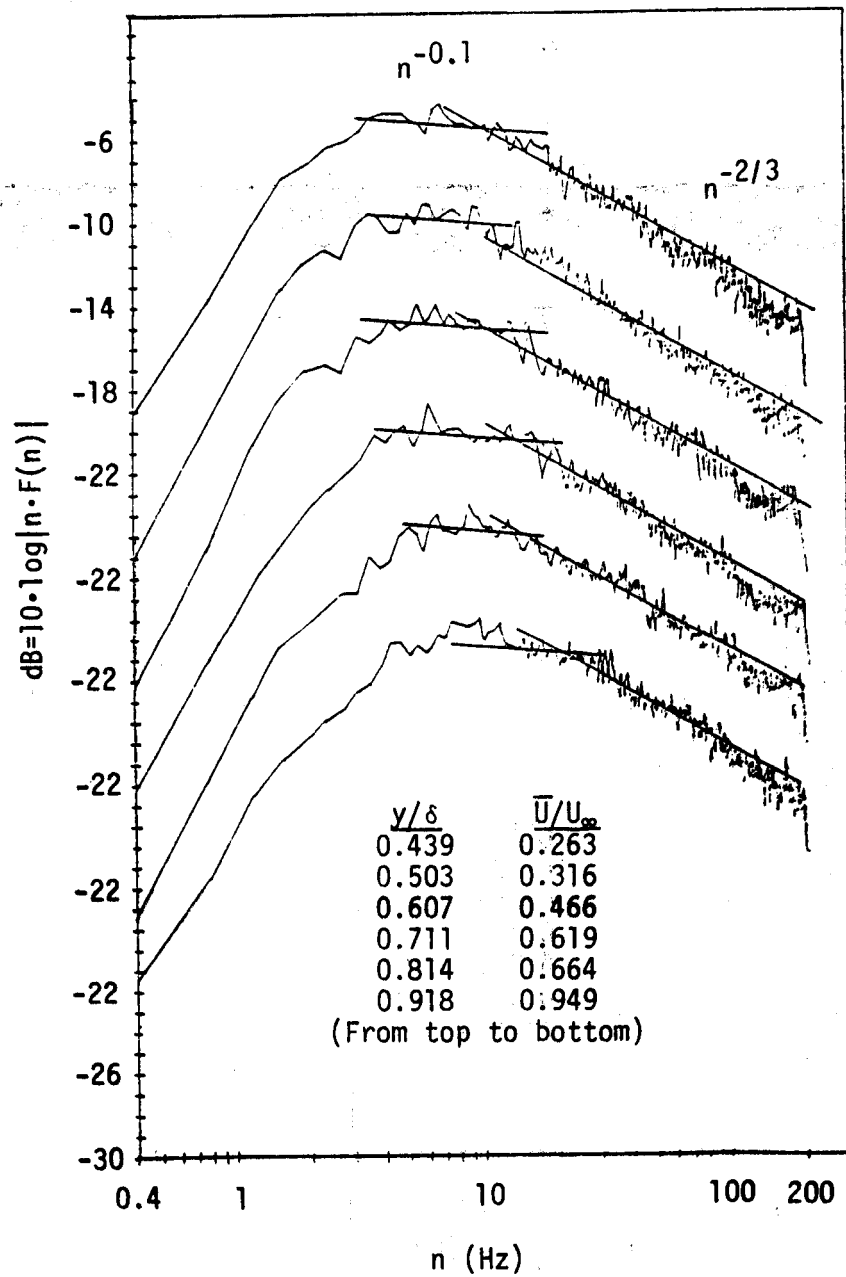
39

Figure 15: Velocity spectra for the downstream x location of 3.970 m. (The parameter $2\pi\delta^*/U_\infty = 0.0734$ sec., also note the displaced ordinates)

Figure 16: Velocity spectra for the downstream x location of **4.340 m.** (The parameter $2\pi\delta^*/U_\infty = 0.0996$ sec., also note the displaced ordinates)
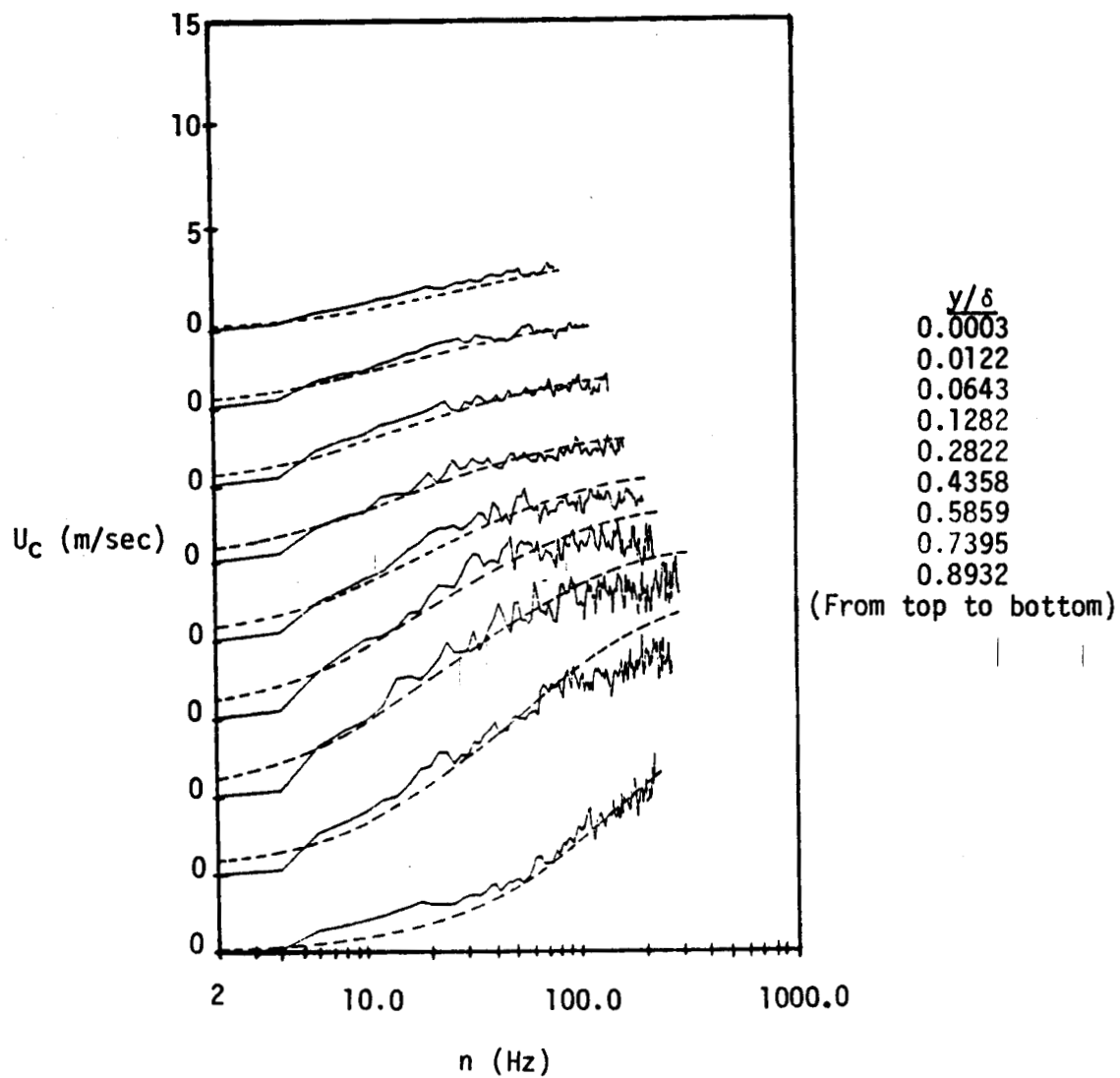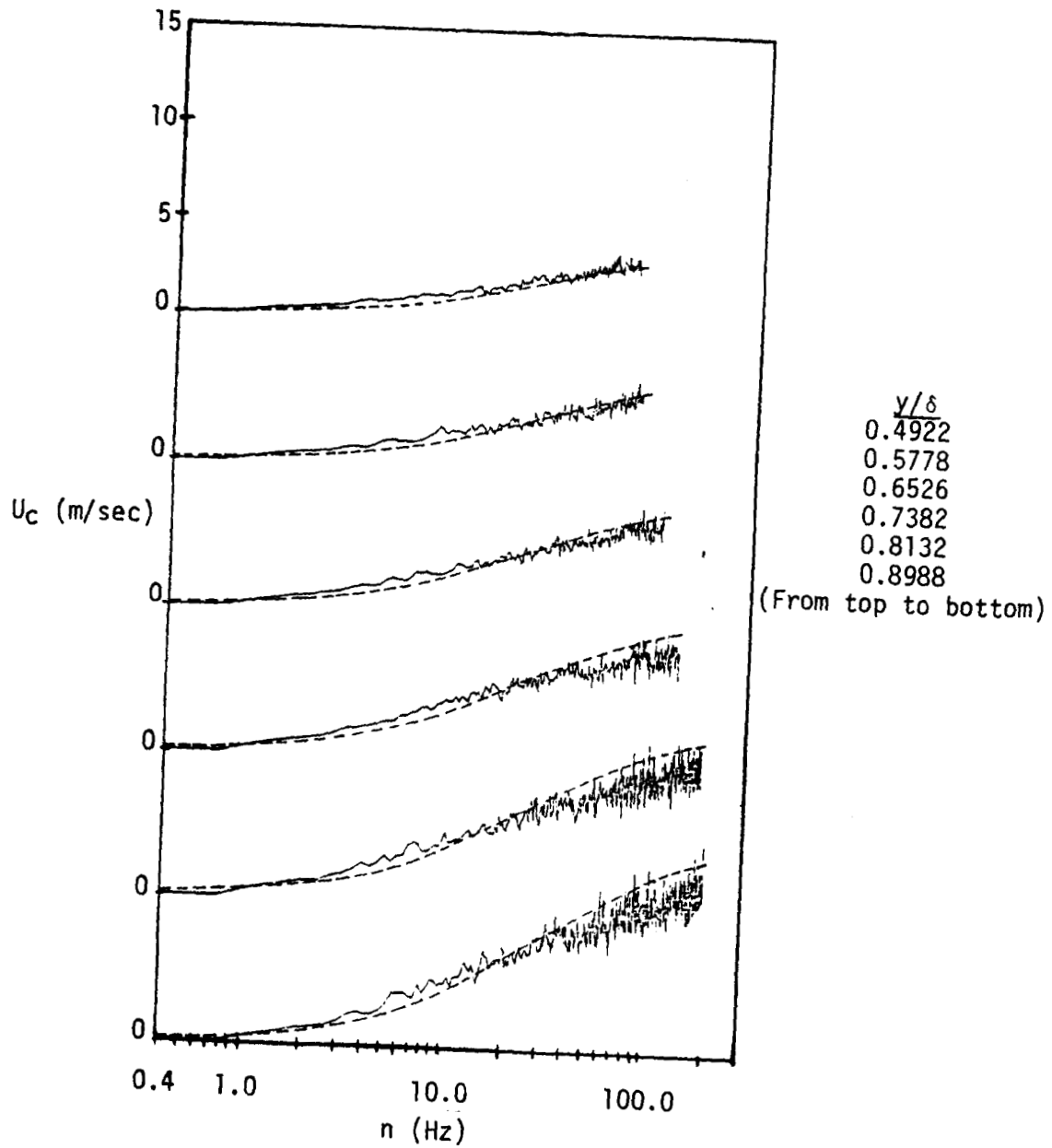
$$U_C \text{ (m/sec)}$$

y/δ
0.0003
0.0122
0.0643
0.1282
0.2822
0.4358
0.5859
0.7395
0.8932

(From top to bottom)

n (Hz)

----- Fit of the model equation for each y/δ position

Figure 17: Velocity celerity (U_C) versus frequency (Hz) for the
downstream x location of 3.009 m.
(Note the displaced ordinates)

----- Fit of the model equation for each y/δ position

Figure 18: Velocity celerity (U_c) versus frequency (Hz) for the
downstream x location of 3.970 m.
(Note the displaced ordinates)

Strickland and Simpson (1973) for their separating turbulent boundary layer, the apparent wavespeed increases with increasing frequency. Strickland and Simpson obtained $U_{cn} = \Delta X/\tau$ values at each frequency, where τ is the time delay for the maximum cross-correlation of the two narrow bandpass-filtered signals. The data are shown for coherence values above 0.36, which Heidrick et.al. (1971) found to be the minimum value that reasonably reliable results could be obtained. Figure 19 shows the values of $2\pi n\Delta X/U$ for each y/δ at which the coherence is 0.36. For increasing y/δ, $2\pi n\Delta X/U$ is lower for the same coherence.

At high frequencies we expect that the smallest-scale motions move on the average with a wavespeed equal to the local mean velocity. If the large structures move at a lower velocity, then the defect with the local mean velocity should be proportional to the wavelength. In other words,
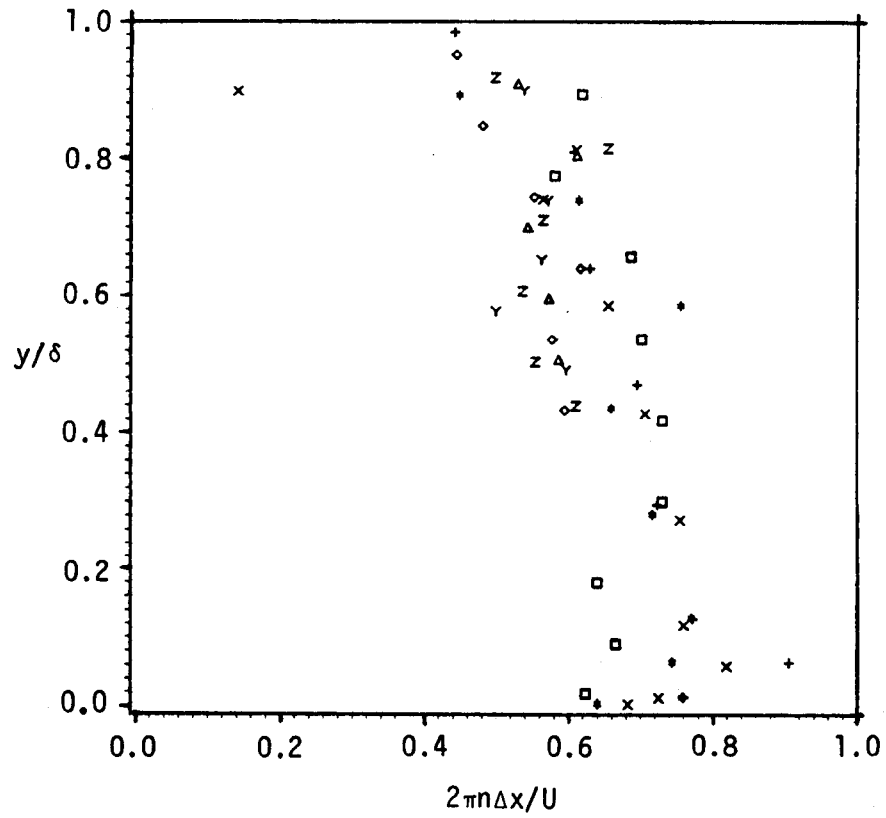
$$\frac{U - U_{cn}}{U} = \frac{U_{cn}}{2\pi nL} \tag{24}$$

where L is some length scale describing the flow at that spatial position. This equation can be rearranged to produce

$$\frac{U_{cn}}{U} = \frac{2\pi nL/U}{\frac{2\pi nL}{U} + 1} \tag{25}$$

which is shown in Figure 20 and will be referred to as the 'model' equation.

Figures 17 and 18 show crude curve fits of the model equation to the lower frequencies. Since U at each position is known, the only adjustable parameter in equation (25) is L. Figures 21 and 22 show the experimental values of L/δ and L/δ^* determined at all available spatial locations.

Figure 19: y/δ versus 2πnΔx/U where R_n=0.6
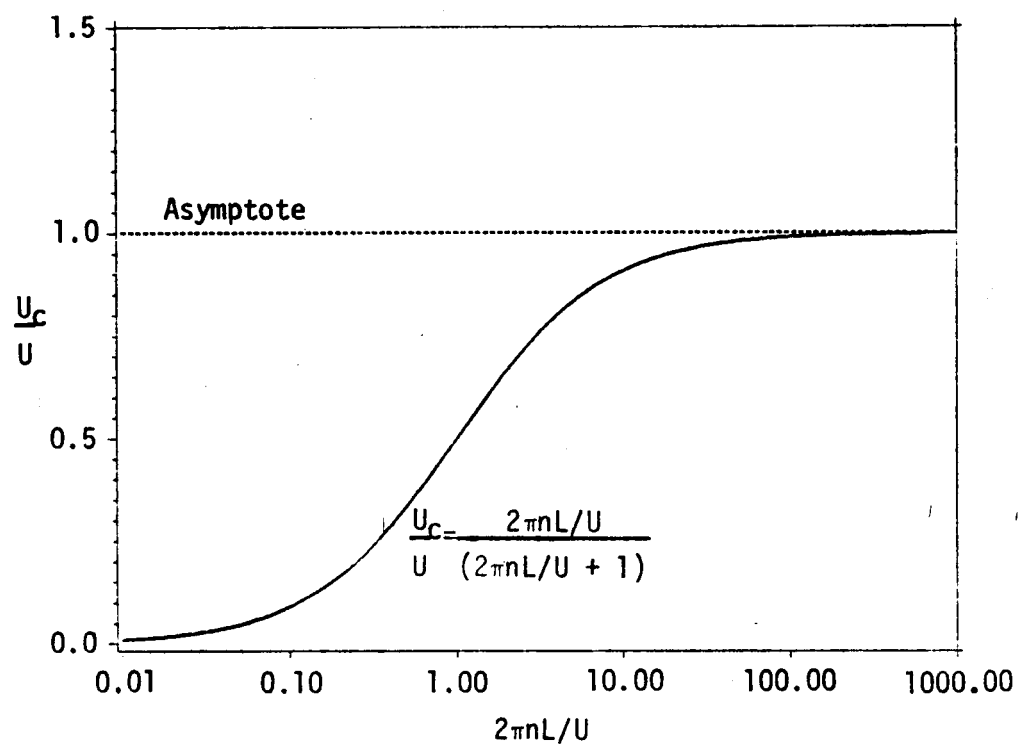
Figure 20: Model equation versus $2\pi nL/U$
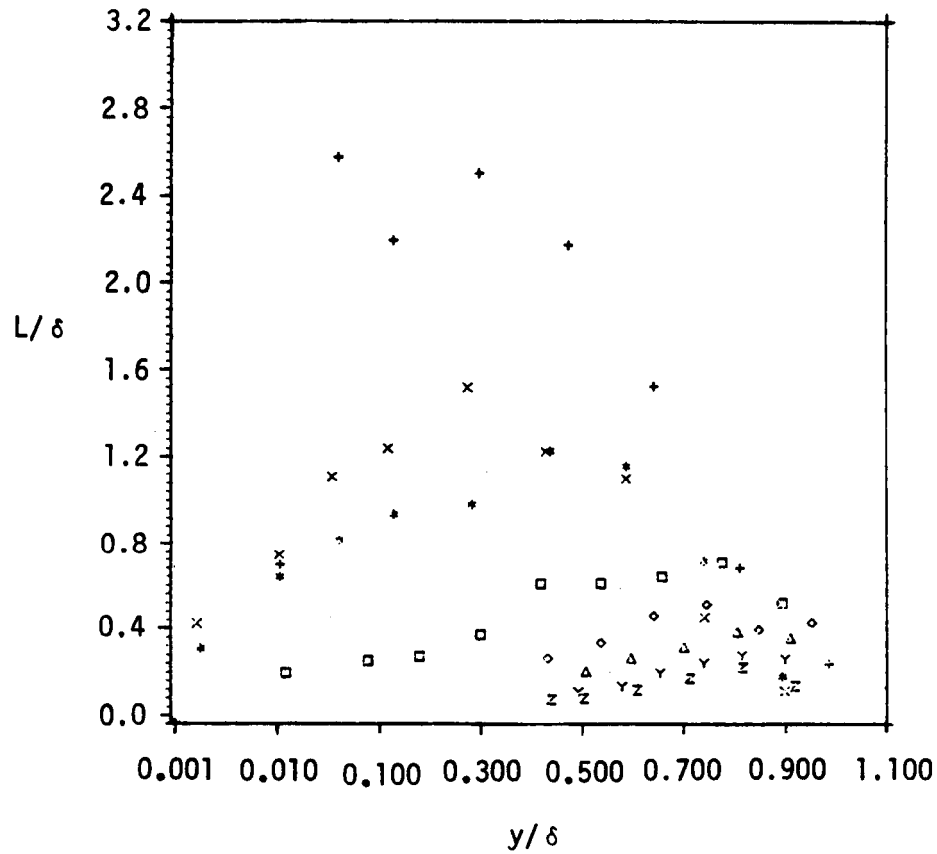
Figure 21: L/δ versus y/δ
(Note the log-linear abscissa)
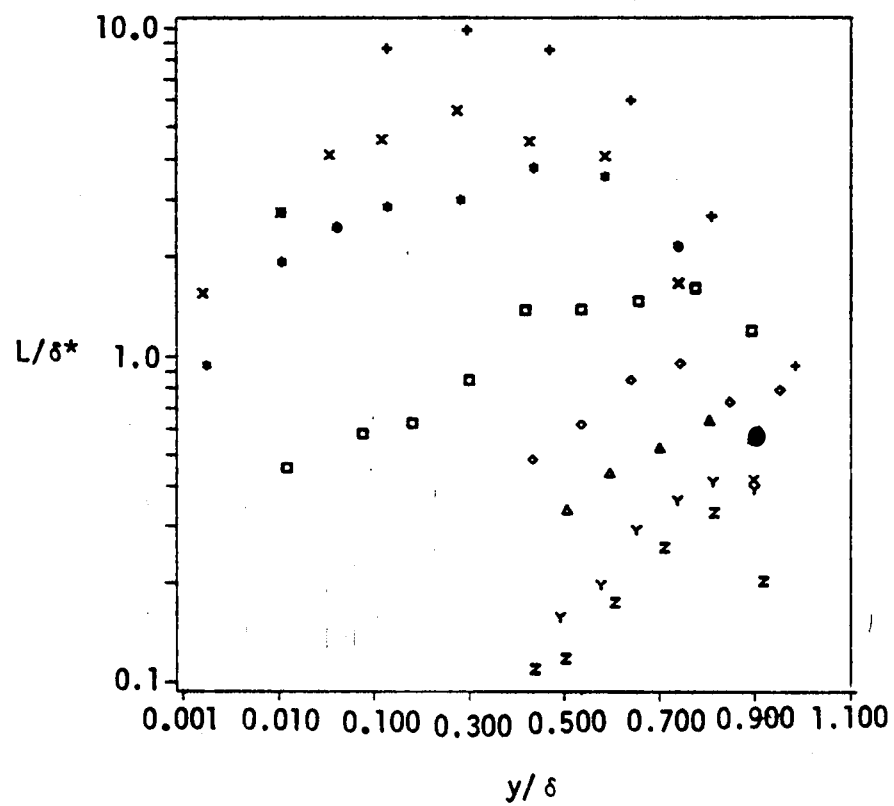
Figure 22: L/δ* versus y/δ
(Note the log-linear abscissa)

These L values are about $\pm$ 30% uncertain due to the subjective nature
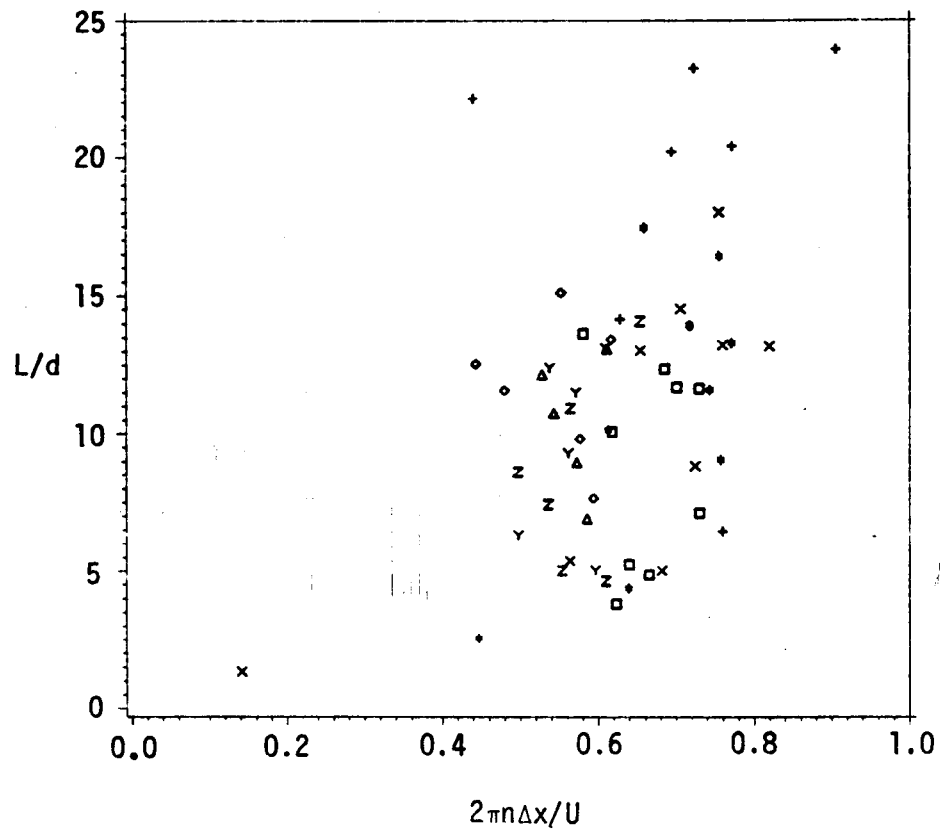
of fitting equation (25) to the mid-range of frequencies.

L decreases with increasing streamwise position, reflecting the

strong deceleration of the large scale structures. At a given stream-

wise position, L increases to a maximum, which lies increasingly farther

from the wall at downstream locations. Downstream of detachment (3.52 m),

no U_{cn} measurements near the wall could be obtained because of the inter-

mittently fluctuating flow direction. Low values of U_{cn} are observed at

$y/\delta = 0.5$, the nearest to wall location without intermittent backflow.

Consequently, L is very low in these nearest to the wall data. Figure 23

shows that $L/\Delta X$ is not a detectable function of $2\pi n\Delta X/U$ when the

coherence is 0.36, which indicates that the level of the coherence for

these data does not strongly influence the results for L.

C. Surface Pressure Fluctuation Spectra

Figure 24 shows surface pressure fluctuation spectra $nF(n)$ for the

adverse pressure gradient region upstream of incipient detachment (ID)

at 3.11 m where there is no intermittent backflow near the wall. As

documented by Simpson et al. (1981 a) for this flow, the wall shear

stress decreases along the flow while the maximum shear stress decreases

slightly. As shown in Table 2, τ_{max}/τ_w and $\overline{p^2}$ increase along the flow.

Figure 25 shows surface pressure fluctuation spectra downstream of

the beginning of intermittent backflow. The maximum shear stress increases

while the mean wall shear stress decreases to zero at detachment at 3.52 m,

and is negative downstream. Figure 26 shows that the bandwidth of the

plateau in the $nF(n)$ curves decreases with streamwise distance until it is

48

Figure 23: L/Δx versus 2πnΔx/U

The y-axis is labeled $dB = 10 \cdot \log |n \cdot F(n)|$ with values $-6, -10, -14, -18, -18, -18, -18, -18, -22, -26, -30$. The x-axis is labeled n (Hz) with values 10, 100, 1000.

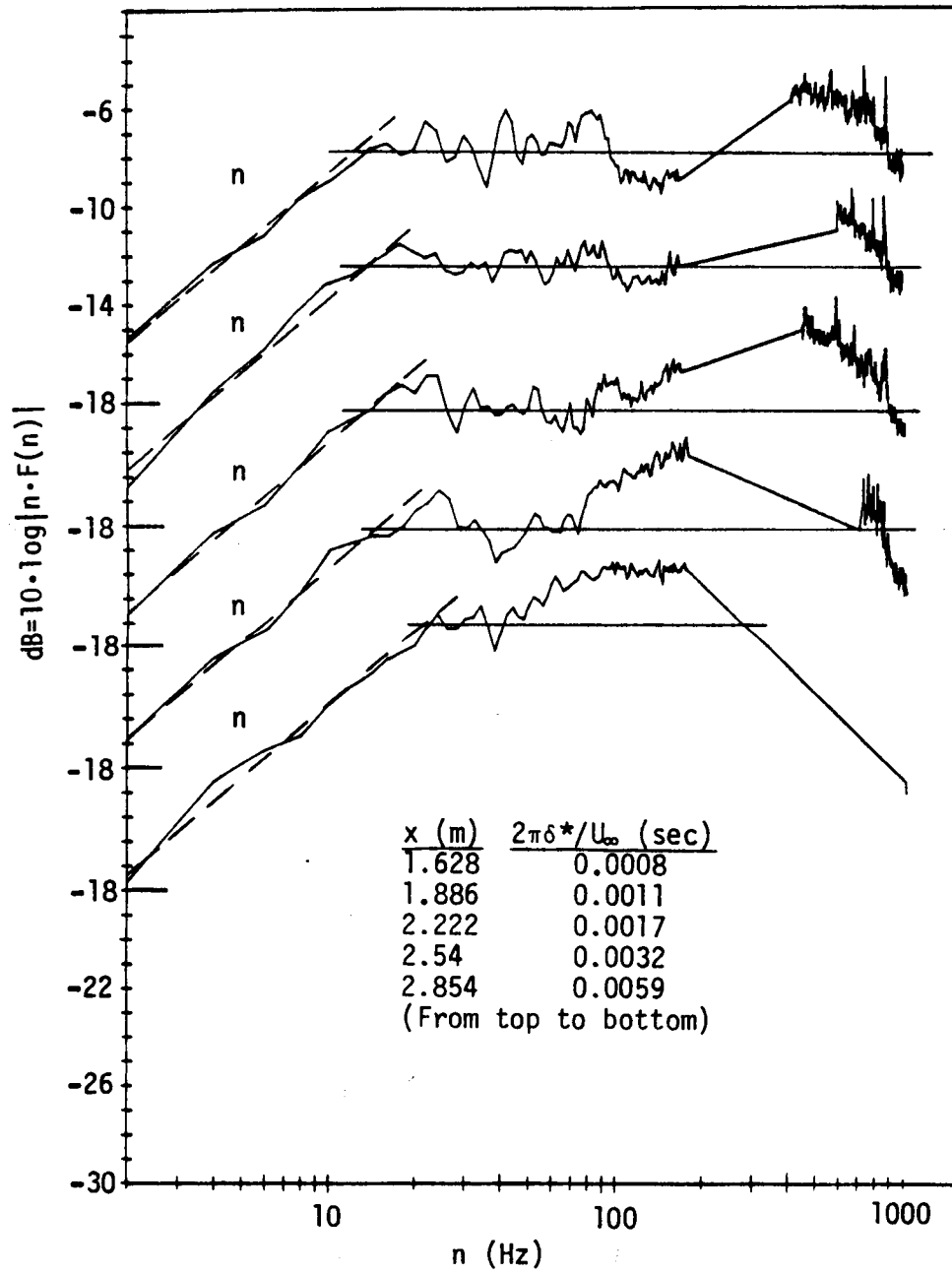| x (m)	$2\pi\delta^*/U_\infty$ (sec)
1.628	0.0008
1.886	0.0011
2.222	0.0017
2.54	0.0032
2.854	0.0059

(From top to bottom)

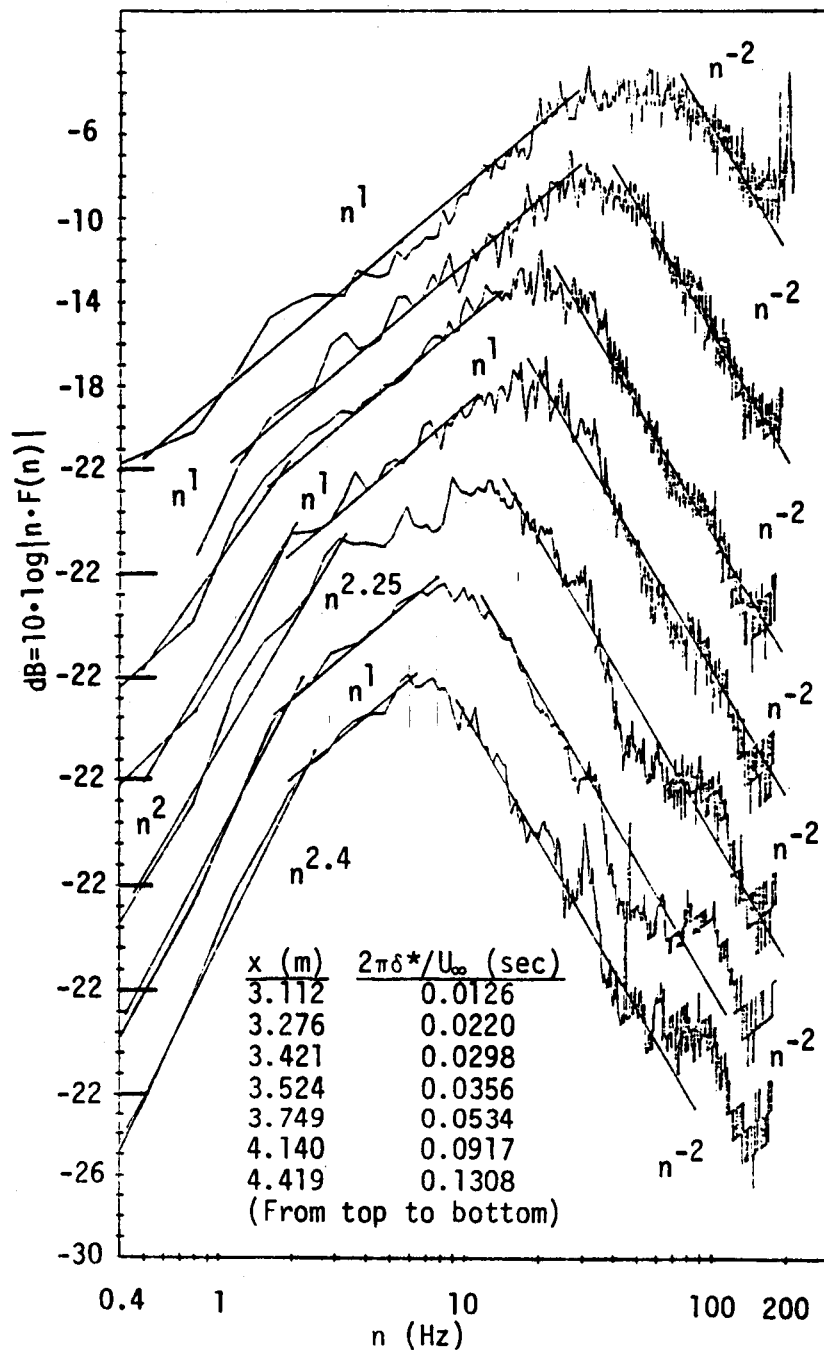Figure 24: Surface pressure spectra upstream of incipient detachment (Note the displaced ordinates)

Figure 25: Surface pressure spectra downstream of incipient detachment
(Note the displaced ordinates)

X location m	U_∞, mps	δ^*, cm	$\dfrac{U_M}{U_\infty}$	$\dfrac{\tau_M}{\tau_W}$	$\overline{p^2}$, Pa^2	$\dfrac{\overline{p^2}}{\tau_M^2}$	$\dfrac{p'}{\tau_M}\left(\dfrac{NU_M}{N_d U_\infty}\right)^{1/3}$	N, cm	$10\log_{10}\left(\dfrac{\Phi(\omega)U_\infty}{\delta^*\tau_M^2}\right)$ at $\omega\delta^*/U_\infty = 1/2$
1.63	21.8	0.28	0.042	1.0	5.00	5.29	—	—	2.01
1.89	21.3	0.38	0.040	1.04	5.45	7.65	—	—	2.31
2.22	20.4	0.55	0.038	1.08	5.87	11.7	—	0.38	3.11
2.54	18.8	0.96	0.042	1.77	6.60	11.7	—	0.81	4.11
2.85	17.0	1.60	0.046	3.08	8.87	16.2	—	1.68	5.51
3.11	15.1	3.05	0.055	—	10.7	15.3	—	4.1	8.01
3.28	14.4	5.08	0.050	—	11.8	31.0	2.32	4.7	11.01
3.42	14.3	6.78	0.058	—	12.0	17.7	1.68	7.4	8.01
3.53	14.0	7.90	0.060	—	12.7	19.0	1.70	6.8	8.01
3.75	13.6	11.6	0.068	—	14.4	14.1	1.78	10.7	9.01
4.14	12.5	18.3	0.078	—	17.3	7.02	1.52	16.5	4.01
4.42	10.7	22.2	0.121	—	17.2	4.41	1.50	20.5	2.01

Table 2. Experimental data presented here for the Simpson et al. (1981 a, b, c) separating turbulent boundary layer.

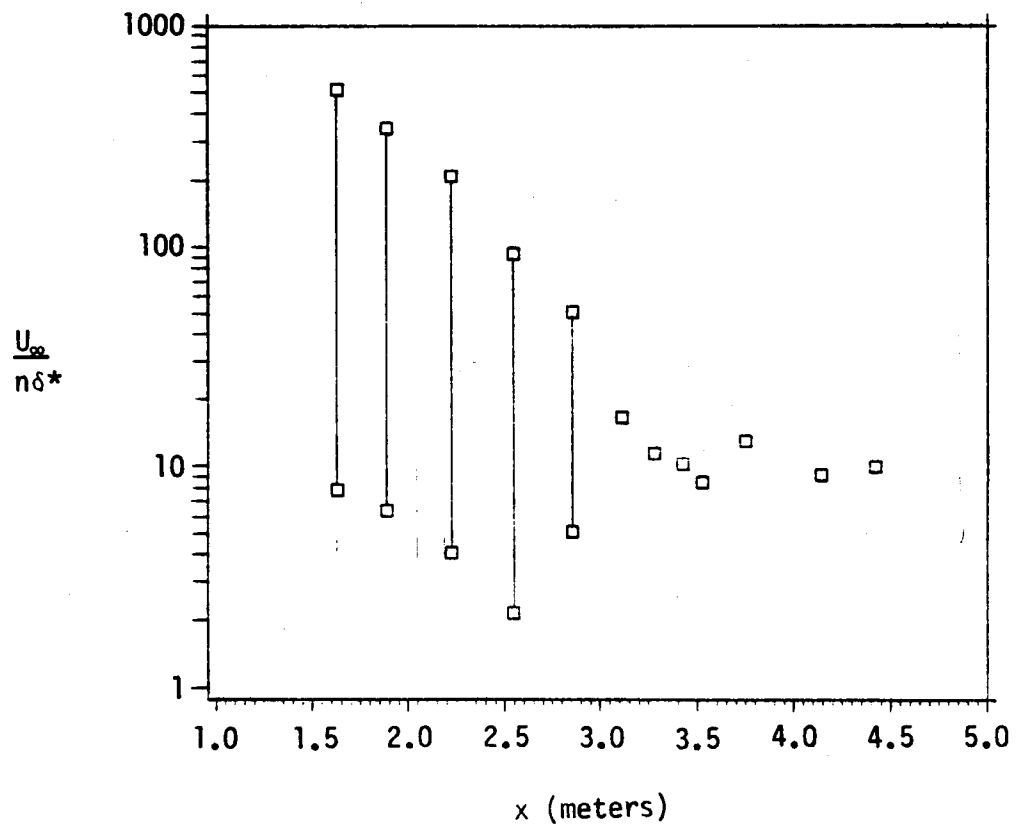Figure 26: Range of n·F(n) plateau for the surface pressure spectra

no longer detectable downstream of incipient detachment.

The results in Figures 24 and 25 were obtained by subtracting the signals from the two microphones that have equal effective signal sensitivities, i.e., equation (16) and the technique described in section IV.C were used. For frequencies below 15Hz, F(n) is about constant upstream of detachment. For higher frequencies less than 150 Hz, nF(n) is about constant upstream of incipient detachment.

Between 150 Hz and 1000 Hz two effects were observed. The vertical and spanwise acoustical waves that are anti-symmetric about the tunnel centerline are additive when the signals are subtracted and equation (16) is used. Consequently, equation (19) was used to obtain the turbulent contributions at those frequencies. The straight lines shown on Figure 24 show the approximate corrected spectrum for that frequency range.

The second effect is a hump in each spectrum. At first glance this is apparently the pinhole-related amplification of a certain frequency range described by Bull and Thomas and discussed in Section II. This effect does not cancel when subtracting the signal from two equally sensitive microphones when using equation (16). Bull and Thomas only examined zero-pressure-gradient cases and concluded that $\frac{\omega \nu}{U_\tau^2} > 0.1$ for this effect to be important. On this criterion, $\omega \nu / U_\tau^2 < 0.1$ for the present data under 1 KHz upstream of incipient detachment, making this pinhole effect appear to be unrelated to the humps in the nF(n) spectra near 500 Hz.

If we re-examine the Bull and Thomas data, we see that the wavelengths that were amplified in their experiments are equal to the pinhole diameter when $1 < \omega \nu / U_\tau^2 < 2$. In other words, when $nd/U_c \approx 1$, spurious amplification of pressure fluctuations occurred for the Bull and Thomas

pinhole data. The present data produce values of $nd/U_c < 0.1$ for the observed humps. Thus, it is reasonable to conclude that the Bull and Thomas pinhole effect is unimportant for these data and that the observed humps are produced by the turbulent flow. If one compares these spectra with the velocity spectra in Figures 5-11, it appears that the low frequency end of each hump coincides closely with the low frequency end of the $n^{-2/3}$ region for the $nF(n)$ velocity spectra.

Figures 27-29 show the spectral data for the attached flow in non-dimensional coordinates. The Corcos (1963) sensor resolution correction was applied to these data and amounted to the order of 1 dB at the higher frequencies. The freestream dynamic pressure has less direct influence on the pressure spectral than the local streamwise maximum shearing stress τ_M. Consequently, Figure 28 shows a tighter correlation of the ordinate values than shown in Figure 27. In both of these figures, the higher frequency portions of the spectra ($\omega\delta_1/U_\infty > 1$) do not correlate well. Figure 29 shows a much better correlation of spectra at all locations upstream of detachment when τ_M is used to non-dimensionalize the frequency as well as $\Phi(\omega)$. The variable $\omega\nu/U_M^2$ for strong adverse pressure gradient cases is analogous to $\omega\nu/U_\tau^2$, which correlates data at the higher spectral frequencies for zero pressure gradient flows. In fact, for zero and favorable pressure gradients $U_M = U_\tau$. As shown in Table 2, there is not much variation of U_M/U_∞ along the attached flow, so $\omega\nu/U_M^2 \sim (\omega\delta_1/U_\infty)(\frac{\nu}{\delta_1 U_\infty})$.

Figure 28 shows that for $\omega\delta_1/U_\infty < 1$, the spectra varies about like $\omega^{-0.7}$, which is observed in the data of Brooks and Hodgson (1981) for a NACA 0012 airfoil and was observed by McGrath and Simpson (1985) for

zero and favorable pressure gradient flows with Re_θ < 5000. Upstream
of the strong adverse pressure gradient region (X < 2.54 m and τ_M/τ_w < 1.5),
the higher frequency spectra vary like ω^{-8}. McGrath and Simpson (1985)
observed a $\omega^{-5.5}$ variation for the highest frequency components. In
the strong adverse pressure gradient region, $\phi(\omega)$ ~ ω^{-3} at the higher
frequencies, which is not shown in Figure 24 but was observed from data
obtained using the 2 KHz range of the FFT that are included in Figures
27-29.

Figure 25 clearly shows the n^{-2} dependence of nF(n) at the higher
frequencies of the detaching flow. This n^{-2} behavior has been observed
in the data of Bull and Thomas for a zero-pressure-gradient flow, Kiya
et al. for a separated forward facing step flow, and Bradshaw, Burton,
and Schloemer for adverse pressure gradient boundary layers. When we
compare Figure 28 and Table 2 with Figure 2, we see that $\phi(\omega)$ has
approximately the same shape and magnitude as for the earlier attached
flow investigations.

Figure 25 shows that the frequency range where F(n) is constant
decreases continuously in the downstream direction. At the lowest
frequencies downstream of detachment, F(n) varies with n to a power
greater than one. Figure 30 shows that the peak frequency of nF(n) and
the n^{-2} high frequency range of the spectra in Figure 25 can be correlated
using the non-dimensional frequency $\omega\delta^*/U_\infty$. The peak occurs at
$\omega\delta^*/U_\infty \approx 0.8$ and the n^{-2} range extends to about 6. Figures 12-16 show
that the peak frequencies of nF(n) for the velocity spectra near the
maximum shearing stress location (y/$\delta \approx$ 0.5) are approximately the same
as peak frequencies shown in Figure 25. The streamwise velocity spectra
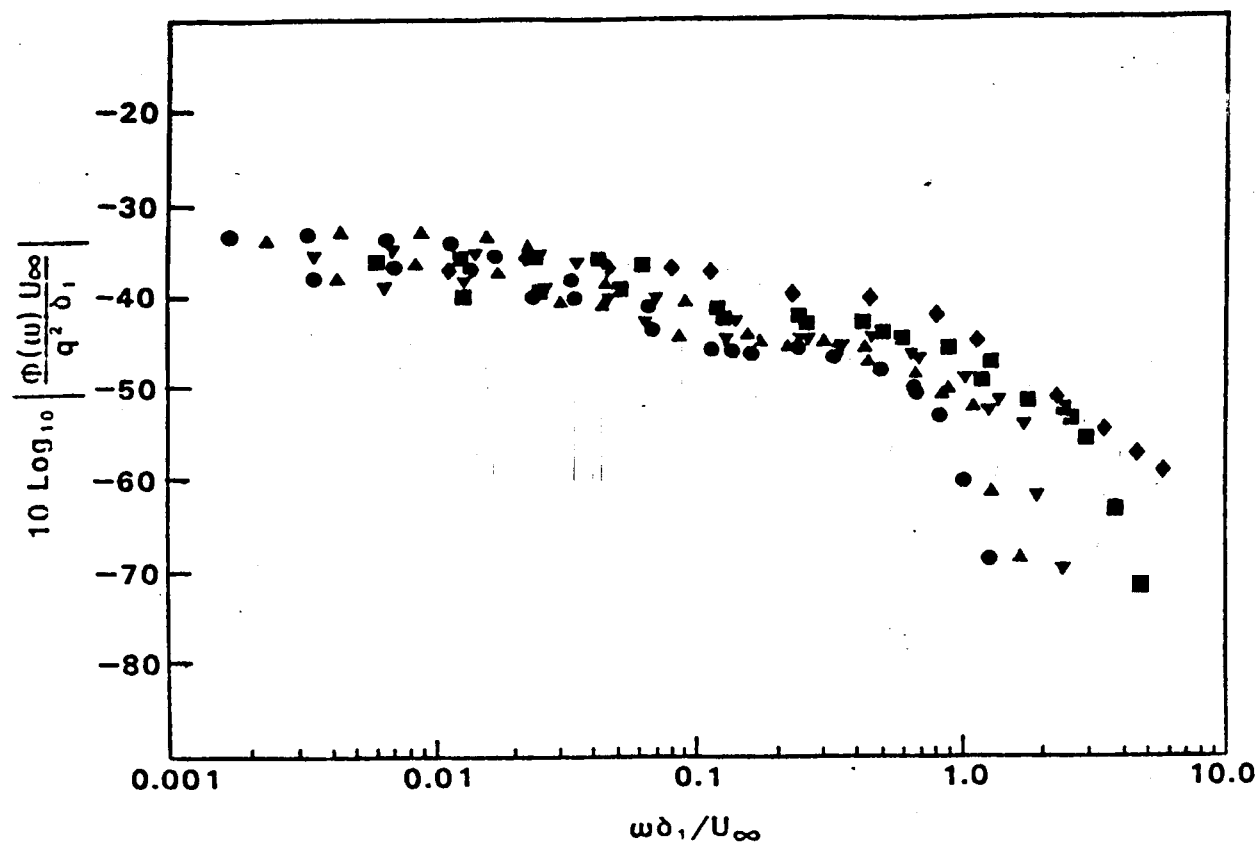in the intermittent backflow region obtained by Simpson et al. (1981 b)

Figure 27: Surface pressure spectra upstream of incipient detachment, normalized on local freestream q, δ_1, and U_∞:   ●, 1.63 m;   ▲, 1.89 m;   ▼, 2.22 m;   ■, 2.54 m;   ◆, 2.85 m.
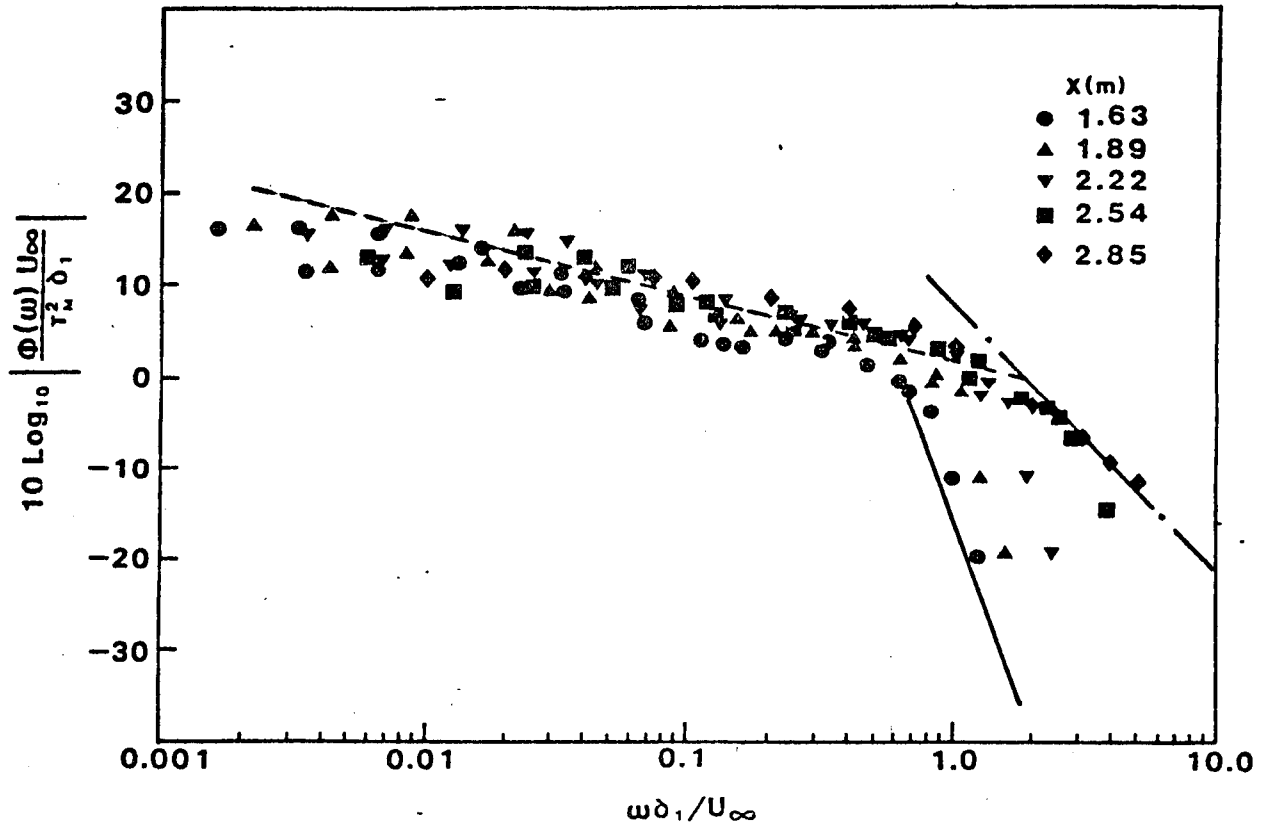
Figure 28: Surface pressure spectra upstream of incipient detachment, normalized on local τ_M, δ_1, and U_∞. Dashed line: $\omega^{-0.7}$ variation; solid line: ω^{-8} variation; broken line: ω^{-3} variation.
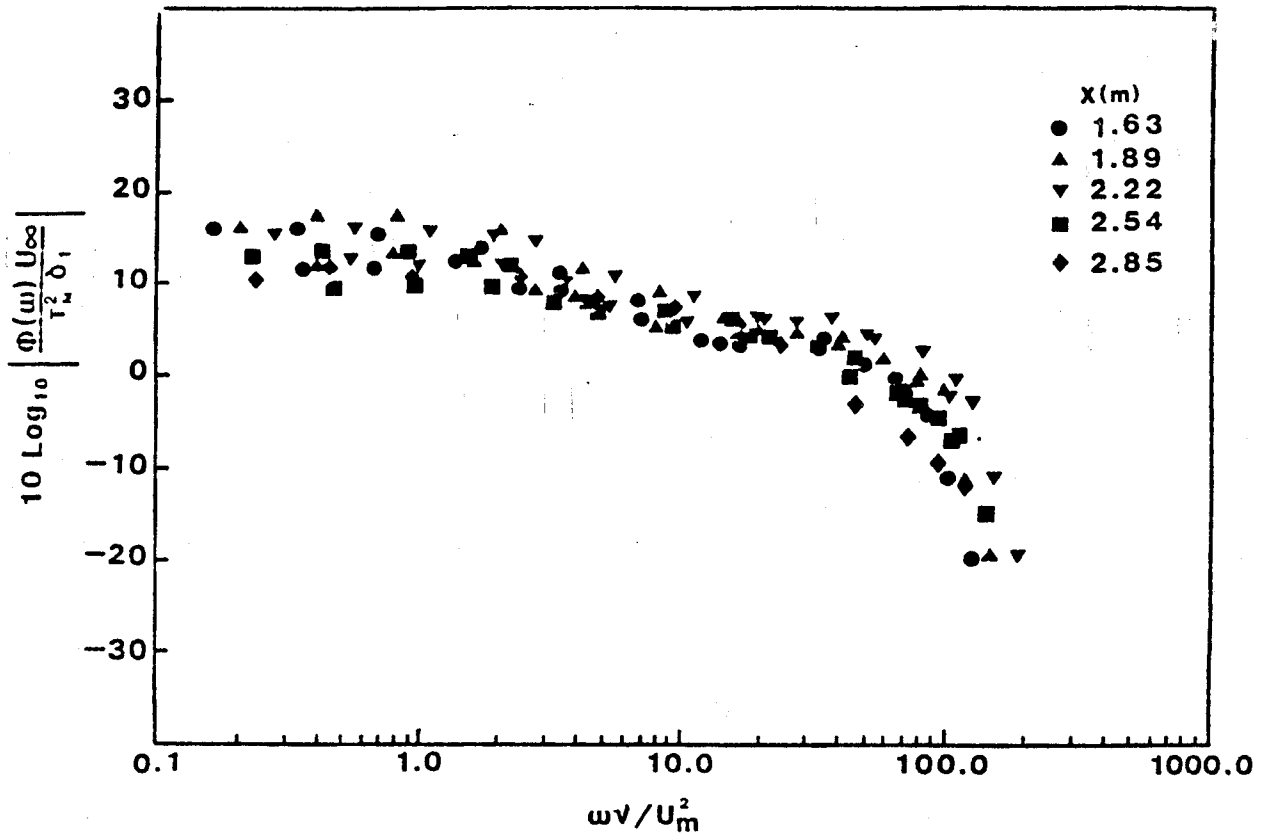
Figure 29: Surface pressure spectra upstream of incipient detachment, normalized on τ_M.
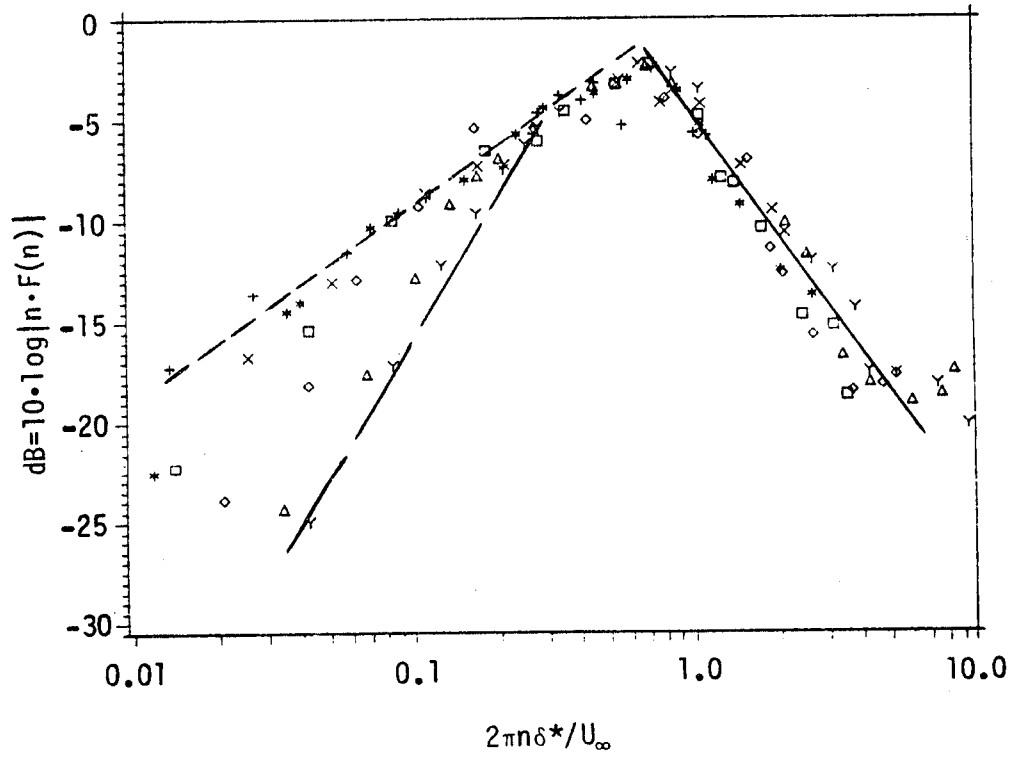
Legend

+	x=3.112 m
X	x=3.276 m
✳	x=3.421 m
□	x=3.524 m
◇	x=3.749 m
△	x=4.140 m
Y	x=4.419 m

Figure 30: Nondimensional surface pressure fluctuation spectra downstream of incipient detachment. Broken line: $\omega^{2.4}$; Dashed line: ω^{1}; Solid line: ω^{-2}.

with a laser anemometer indicate that nF(n) is constant for 0.07 <

$\frac{\omega\delta^{*}}{U_{\infty}}$ < 0.5. This frequency range is below the peak frequency in

Figure 30.

Figures 31 and 32 show the surface pressure spectra downstream of incipient detachment in non-dimensional coordinates. In Figure 31 $\Phi(\omega)$ is normalized on q; this plot masks the true variations at low frequencies that are observed in Figures 25, 30 and 32. Figure 32 shows that normalization on τ_M produces a much tighter correlation for $\omega\delta_1/U_{\infty}$ > 1. The Corcos (1963) microphone resolution correction was not applied to these data because large wavelength motions dominate the detached flow and require negligible correction. Furthermore, and more importantly, the instantaneous flow reversal contains small and large wavelength motions that as yet cannot be related to specific frequencies.

Figure 33 shows the rms pressure values p' computed from these data and normalized on the reference inlet dynamic pressure, the local wall shear stress τ_W, and the local maximum shear stress τ_M. The uncertainty of p' is about ± 20%. Although p' increases along the flow, p'/τ_M increases to detachment and then decreases. At X=1.63 m at the end of the favorable pressure gradient region, p'/τ_W=2.3 which is in very good agreement with values obtained by McGrath and Simpson (1985) for a favorable pressure gradient flow at the same Re_θ.

D. Surface Pressure Fluctuation Celerities

Figures 34 and 35 show the square root of the coherence for two microphones whose pinholes are separated ΔX in the streamwise direction. These results were obtained using equations (20-22). The values of γ
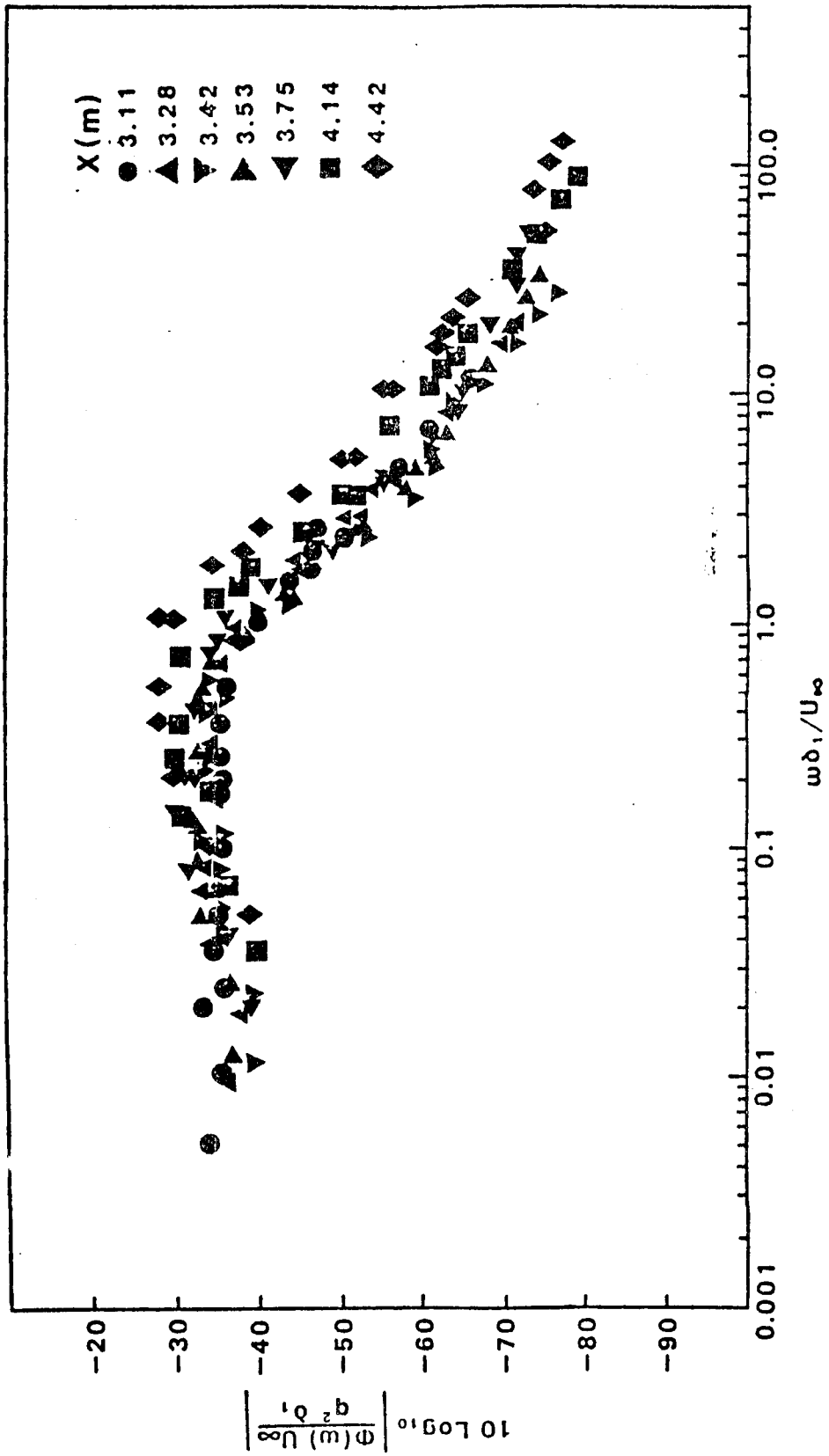
Figure 31: Surface pressure spectra downstream of incipient detachment
normalized on q, δ_1, and U_∞.
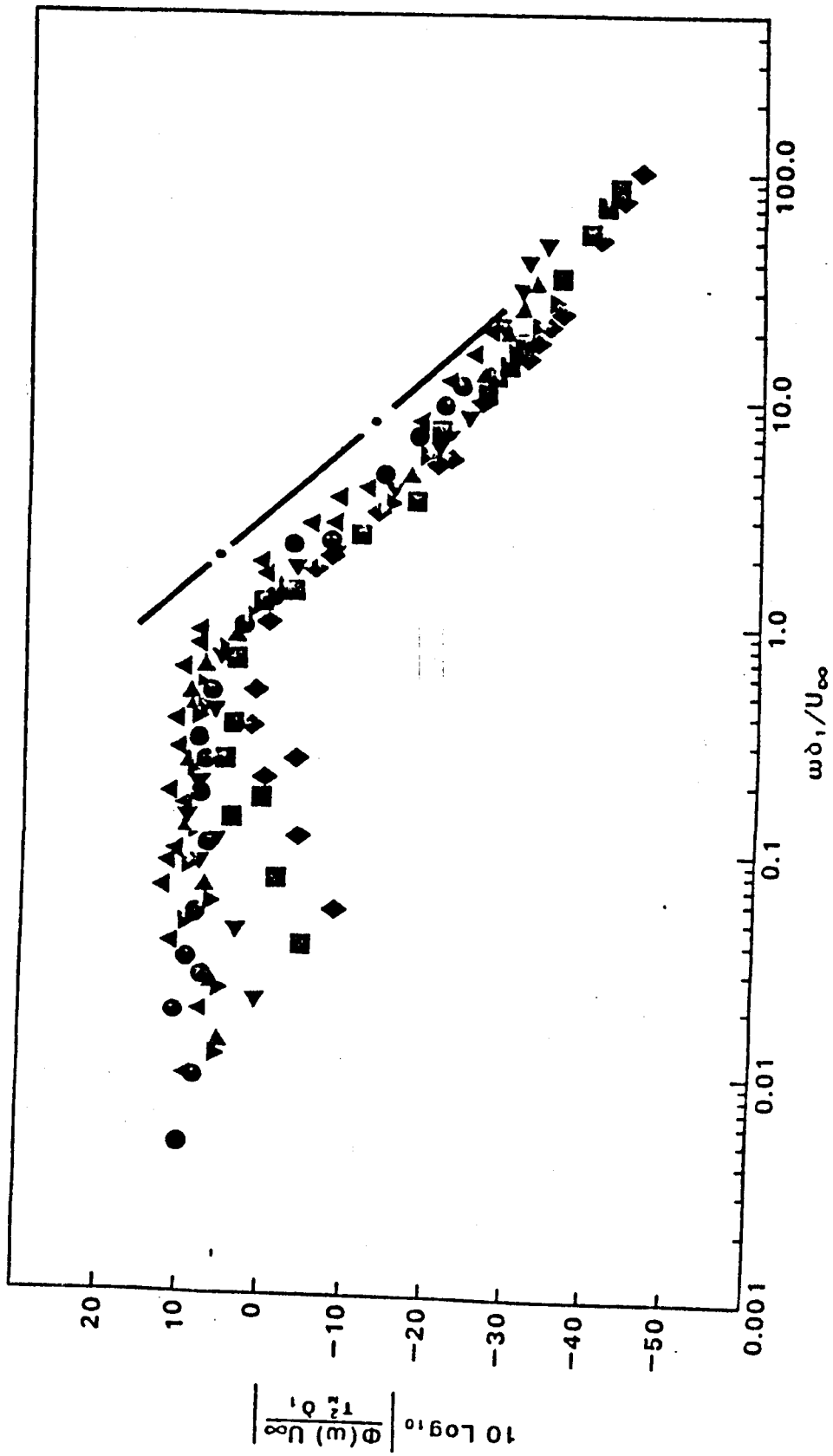
Figure 32: Surface pressure spectra downstream of incipient detachment, normalized on τ_M. Broken line: ω^{-3} variation.
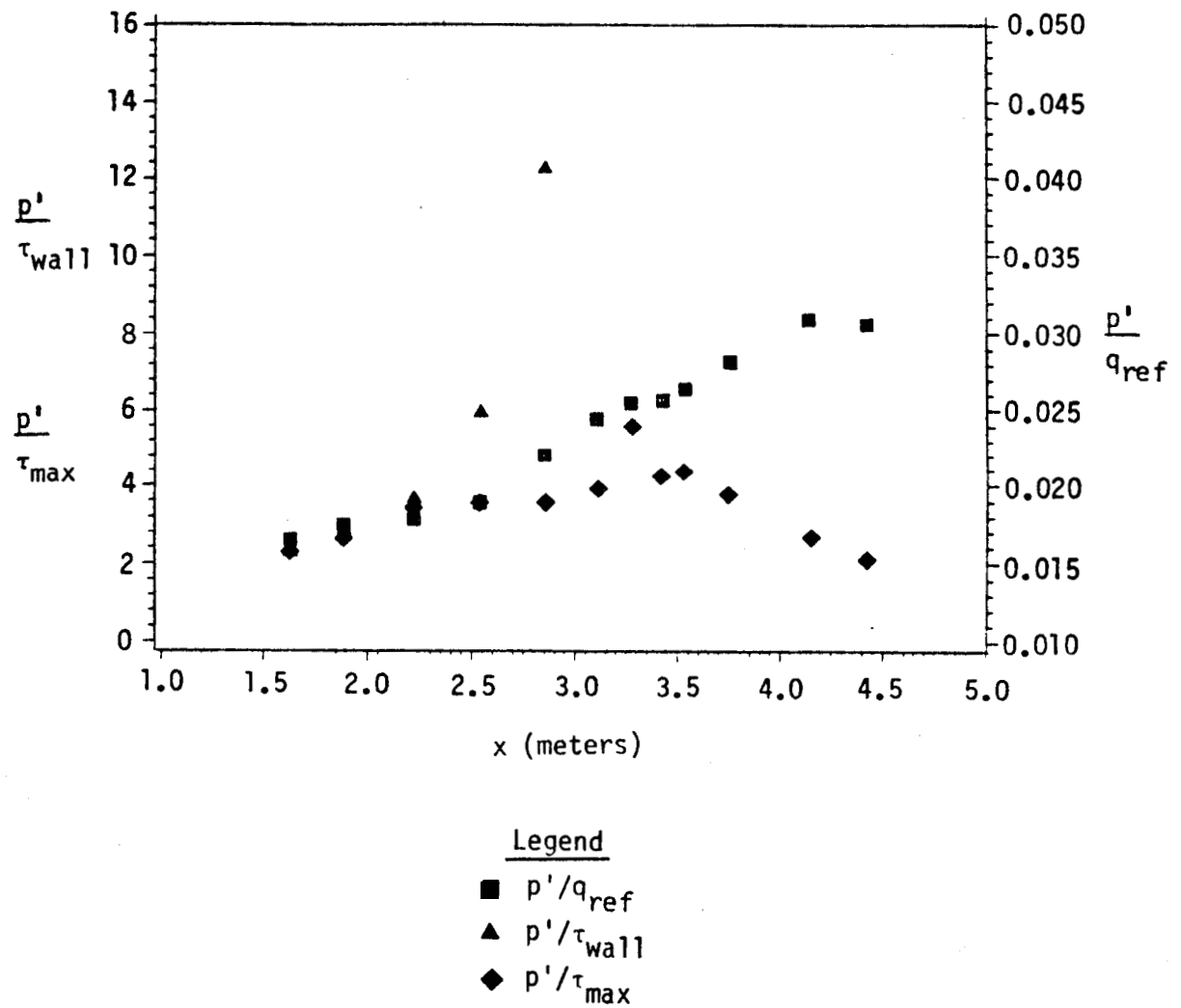
Figure 33: Streamwise distribution of p'/q_{ref}, p'/τ_{wall}, and p'/τ_{max}.

are low, indicating a large decay in similarity of the pressure signals between microphones. Like the data of Brooks and Hodgson and of Hahn, γ increases with frequency to a maximum in the frequency range where $nF(n)$ is a maximum for the locations upstream of incipient detachment. At higher frequencies γ drops to very low values.

Corcos (1963) proposed that the cross spectrum in the lateral and longitudinal directions decay exponentially with the phase angle ϕ. In terms of the square root of the coherence

$$\gamma = \exp \left(-K_1\phi - K_3 \left(\frac{\Delta Z}{\Delta X}\right)\phi\right) \tag{26}$$

Upstream of incipient detachment $K_1=0.12$, as shown in Figure 34. At the lower values of ϕ, agreement with equation (26) is poor, but Brooks and Hodgson show a similar behavior. This value of K_1 seems low for a strong adverse pressure gradient flow in view of Schloemer's (1967) result that K_1 is greater for adverse pressure gradients than for zero pressure gradients. Zero pressure gradient values of 0.11 to 0.23 have been reported (Corcos, 1963; McGrath and Simpson, 1985; Brooks and Hodgson, 1981).

After some intermittent backflow begins downstream of incipient detachment, the value of K_1 appears to drastically increase, as shown in Figures 34 and 35. A $K_1=0.75$ approximately describes the data at X=3.28 m and 3.53 m; $K_1 \sim 1.0$ at X=4.14 m. These values of K_1 are close to the values of K_3 near 0.75 reported for the lateral or spanwise decay of γ for zero and adverse pressure gradient attached boundary layers (Corcos, 1963; McGrath and Simpson, 1985; Brooks and Hodgson, 1981;

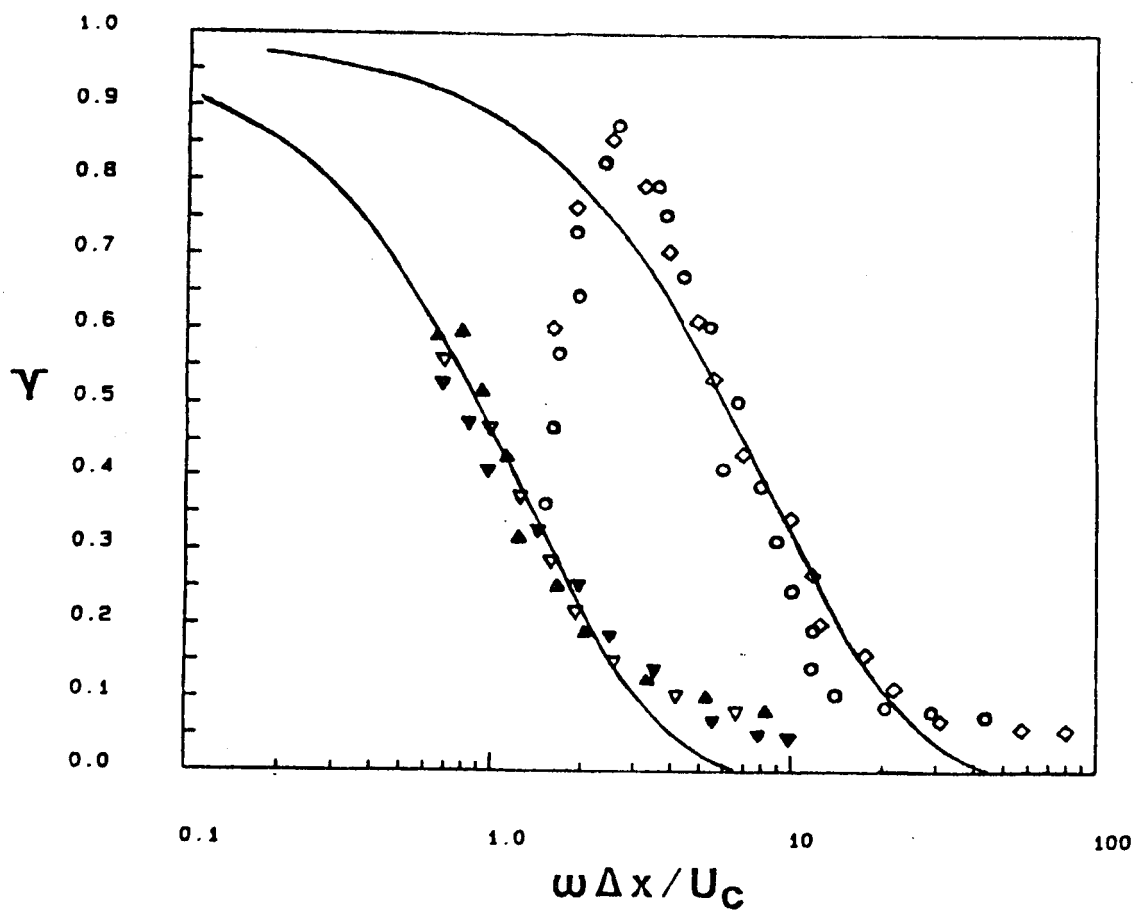Figure 34: Square root of streamwise coherence upstream of and in the detachment zone.

Upper line: $K_1 = 0.12$ in equation (26)

Lower line: $K_1 = 0.75$ in equation (26)

$\bigcirc$, 2.22 m, $\Delta X/\delta_1 = 2.55$; $\diamondsuit$, 2.85 m, $\Delta X/\delta_1 = 0.28$;

3.28 m: $\triangledown$, $\Delta X/\delta_1 = 0.28$; $\blacktriangle$, $\Delta X/\delta_1 = 0.44$;

$\blacktriangledown$, $\Delta X/\delta_1 = 0.60$.
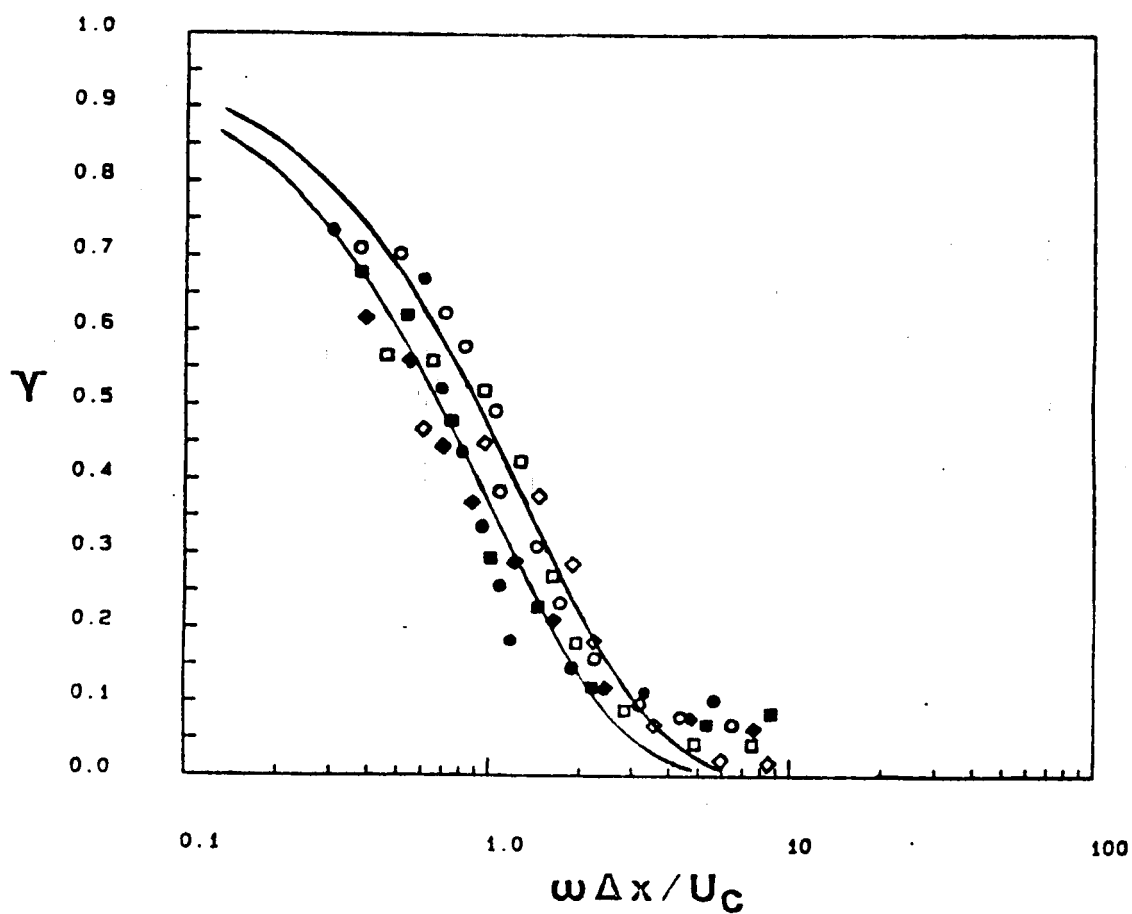
Figure 35: Square root of streamwise coherence downstream
of detachment. Top line, equation (26) with
K_1 = 0.75; Bottom line, equation (26) with K_1 = 1.00.
At 3.53 m: $\bigcirc$, $\Delta X/\delta_1$ = 0.177; $\square$, $\Delta X/\delta_1$ = 0.283;
$\diamondsuit$, $\Delta X/\delta_1$ = 0.383. At 4.14 m: $\bullet$, $\Delta X/\delta_1$ = 0.076;
$\blacksquare$, $\Delta X/\delta_1$ = 0.122; $\blacklozenge$, $\Delta X/\delta_1$ = 0.165.

Figure 36: Pressure fluctuation celerity: ▲, 2.22 m;
● , 2,85 m; ■, 3.28 m; ◆, 3.53 m; ◇,
4.14 m. Solid lines: results from equation
(14) for first three locations. Note displaced
ordinates.

Blake, 1970; Burton, 1973). This suggests, as does the flowfield data, that the intermittent backflow destroys the streamwise coherence of pressure fluctuations.

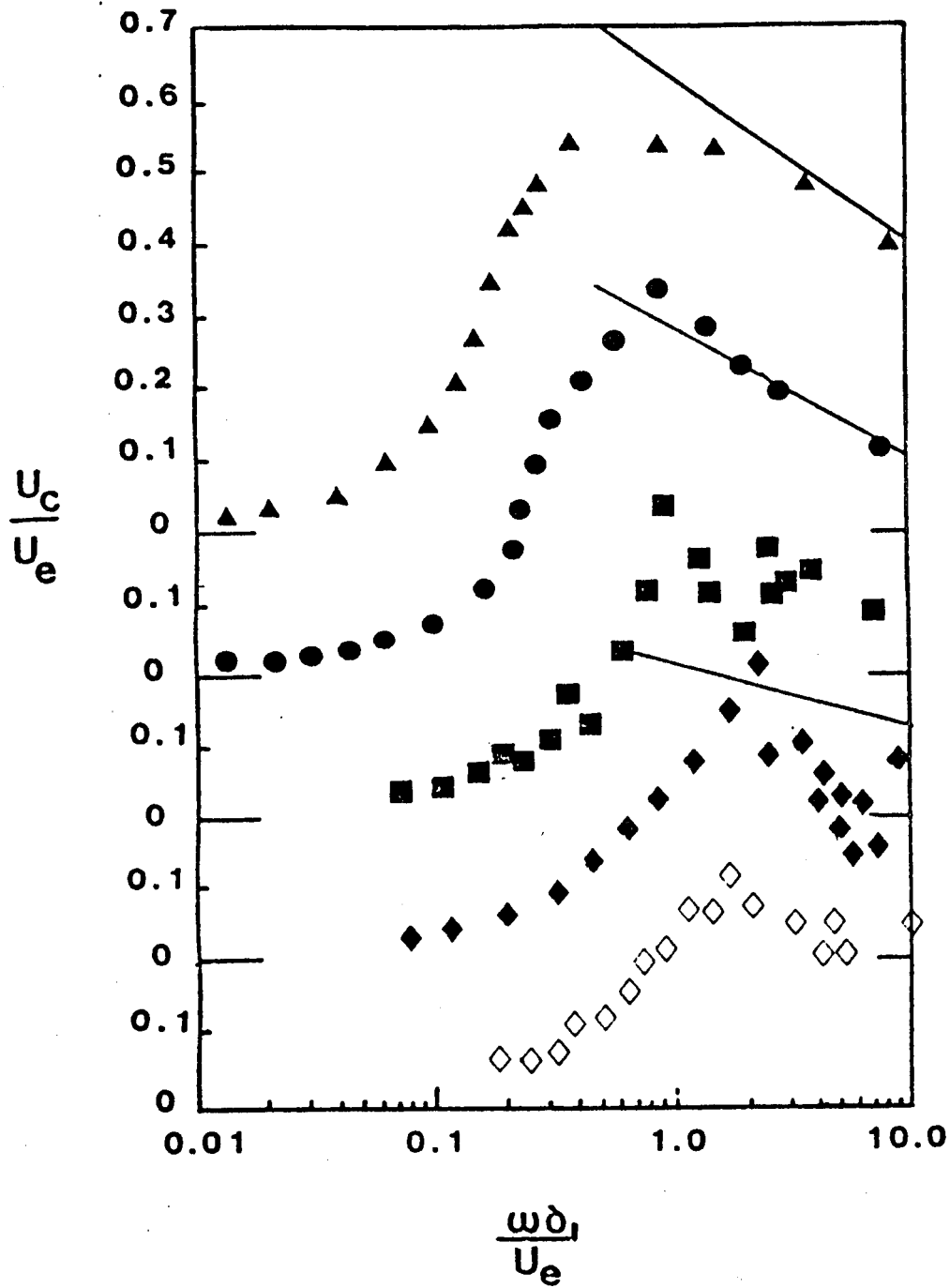Figure 36 shows that upstream of incipient detachment, U_c increases with increasing frequency till near $\omega\delta_1/U_\infty = 1$ as observed by Brooks and Hodgson. U_c decreases at higher frequencies and agrees asymptotically with equation (14) for the inner-outer overlap region. After the beginning of intermittent backflow, U_c no longer agrees with equation (14) and very low values of U_c are observed. The experimental uncertainty on U_c is about ± 0.05.

VI. DISCUSSION, SUMMARY AND CONCLUSIONS

The streamwise velocity fluctuation spectra and celerities for this flow possesses expected features. There is no effect of wind tunnel acoustic noise on the velocity spectra. Near the wall upstream of detachment, $nF(n)$ is nearly constant over a frequency range while a definite $F(n) \sim n^{-5/3}$ inertial subrange region is observed at higher frequencies. The frequencies of the energy-containing motions decrease as detachment is approached, as observed by Simpson et al. (1977, 1981 b).

As observed by Strickland and Simpson (1973), the celerity U_{cn} increases with frequency till it approaches the local U asymptotically. The simple crude model equation (25) was observed to fit U_{cn} along this flow. Unfortunately, the length scale L in this model equation is not known a priori. It was observed to decrease with streamwise position and to reach a maximum at a given streamwise position increasingly farther from the wall. Downstream of the beginning of intermittent backflow, no

U_{cn} measurements near the wall can be made because of the ambiguity of the flow direction.

At the end of the favorable pressure gradient region far upstream of incipient detachment, $p'/\tau_w = 2.3$, which is in very good agreement with values obtained by McGrath and Simpson (1985) for a favorable pressure gradient flow at the same Re_θ. The ratio $\overline{p^2}/\tau_M^2$ is substantially larger for the attached strong adverse pressure gradient part of the present flow than in the investigations listed in Table 1. As discussed in Section II, $\overline{p^2}/\tau_M^2$ is proportional to the ratio of streamwise length scale to length scales in other directions α. The integral length scale data of Chehroudi and Simpson (1983) show that α is about 2.5 for this flow, which is in agreement with the Schubauer and Klebanoff (1951) results for α in their separating flow. Thus, the present results for $\overline{p^2}/\tau_M^2$ upstream of detachment appear plausible. This apparent importance of α on $\overline{p^2}$ suggests that space-time velocity correlations should be obtained in future experiments to determine integral length scales.

Downstream of detachment, $\overline{p^2}$ continues to increase, although p'/q_{ref} does not reach values of 0.04 to 0.1 that were observed by Mabey (1972) for step-induced separation and reattachment flows. The ratio p'/τ_M increases to detachment and then decreases downstream. The level of p'/τ_M for these data seems reasonable since Kiya et al. (1982) observed values of $p'/\tau_M \simeq 10$ for a forward-facing step flow. This decrease appears to be due to the fact that the pressure-fluctuation-producing motions move increasingly away from the wall downstream of detachment.

Both the turbulence-mean shear interaction and the turbulence-turbulence interaction in the pressure fluctuation source term, equation

(2),   are important for detached flows. Velocity fluctuations are
as large as mean velocities in the backflow. Reynolds shear stresses
and their gradients are large away from the wall. Thus the largest
pressure fluctuations are not at the wall in a detached flow, but must
be near the middle of the shear layer. Equation (3) indicates that
$\vec{p}(x)$ on the wall must decrease if the source q moves away from the wall.
Table 2 shows that the distance from the wall to the maximum shear
location, N, increases rapidly downstream of detachment.

In order to try to correlate this effect a modified version of
equation (13) was used. First, N/δ^* is almost constant downstream of
detachment and $(U_\infty/U_M)^{1/3}$ does not vary enough to correlate p'/τ_M. As
shown in Table 2,

$$\frac{p'}{\tau_M} \left(\frac{NU_M}{N_dU_\infty}\right)^{1/3} \approx 1.64 \pm 8\% \tag{27}$$

where N_d is the distance of the maximum shear stress location from the
wall at detachment.

The spectra for $\overline{p^2}$ substantially agree with other investigations.
Upstream of incipient detachment, $\omega\Phi(\omega)$ is nearly constant over a
frequency range that decreases as detachment is approached. At lower
frequencies $\Phi(\omega)$ varies like $\omega^{-0.7}$; at higher frequencies $\Phi(\omega)$ varies
with ω^{-3}. Downstream of the beginning of intermittent backflow, $\omega\Phi(\omega)$
has a peak near $\omega\delta^*/U_\infty \approx 0.8$ and a ω^{-2} range at higher frequencies.
For lower frequencies, $\omega\Phi(\omega)$ varies with ω near the beginning of
intermittent backflow; farther downstream this low frequency range
varies with $\omega^{2.4}$.

The coherence of the pressure fluctuation producing motions remains high in the streamwise direction upstream of incipient detachment but drops drastically with the beginning of intermittent backflow. The streamwise coherence level looks much like that for the spanwise direction for attached flows.

At low frequencies, both upstream and downstream of detachment, U_{cn} celerity results are reasonable and agree qualitatively with other available data. Upstream of detachment at high frequencies the data agree asymptotically with the overlap region celerity equation (14). The relatively large size of the two microphones used in this work prevented celerity measurements at closer spacings. As discussed in Section II, one should obtain $U_{cn}(k,\omega)$ in future work by obtaining the Fourier transform of frequency-filtered spatial correlations, as done by Bradshaw (1967) and Wills (1970). Downstream of the beginning of intermittent backflow, the instantaneous wavespeed U_{cn} can be both positive and negative for sufficiently high frequencies. Thus, the long-time-averaged U_{cn} is lower than upstream for these frequencies.

From the perspective of using pressure fluctuation data to calculate farfield noise, one should probably locate the effective pressure fluctuation sources along or near the locus of the maximum shear stress position. The pressure-fluctuation-producing motions are concentrated in this region. The celerities of these fluid motions are probably close to those for the pressure fluctuations in this region.

This hypothesis is consistent with the idea of placing the effective pressure fluctuation sources on the flow surface for low pressure gradient

flows, since in these cases the maximum velocity gradients and shear stresses are at or very close to the wall. Since it is not possible to accurately measure pressure fluctuations within the turbulent separated flow, measurements of the farfield pressure fluctuation and the wall measure fluctuation should be used to estimate the effective pressure fluctuations at the maximum shearing stress location.

REFERENCES

Blake, W. K. (1970) "Turbulent Boundary Layer Wall Pressure Fluctuations on Smooth and Rough Walls," J. Fluid Mech., 44, pp. 637f.

Bradshaw, P. (1967) "Inactive Motion and Pressure Fluctuations in Turbulent Boundary Layers," J. Fluid Mech., 30, p. 241f.

Brooks, T. F. and Hodgson, T. H. (1981) "Trailing Edge Noise Prediction from Measured Surface Pressures," J. Sound and Vibration, 78, pp. 69-117.

Brooks, T. F. and Schlinker, R. H. (1983) "Progress in Rotor Broadband Noise Research," Vertica, 7, pp. 3f.

Bull, M. K. (1967) "Wall Pressure Fluctuations Associated with Subsonic Turbulent Boundary Layer Flow," J. Fluid Mech., 28, pp. 719f.

Bull, M. K. and Thomas, A. S. W. (1976) "High Frequency Wall-Pressure Fluctuations in Turbulent Boundary Layers," Physics Fluids, 19, pp. 597-599.

Burton, T. E. (1973) "Wall Pressure Fluctuations at Smooth and Rough Surfaces Under Turbulent Boundary Layers with Favorable and Adverse Pressure Gradients," Acoustics and Vibration Lab. MIT. Rpt. 70208-9.

Chehroudi, B. and Simpson, R. L. (1985) "Space-Time Results for a Separating Turbulent Boundary Layer Using a Rapidly Scanning Laser Anemometer," J. Fluid Mech., 160, pp. 77-92.

Coles, D. E. and Hirst, E., editors (1969) Computation of Turbulent Boundary Layers - 1968 AFOSR-IFP-Stanford Conference, Stanford Univ. Dept. Mech. Eng.

Corcos, G. M. (1963) "Resolution of Pressure in Turbulence," The Journal of the Acoustical Society of America, 35, pp. 192-199.

East, L. F. and Sawyer, W. G. (1979) "An Investigation of the Structure of Equilibrium Turbulent Boundary Layers," AGARD CP-271, paper 6.

Favre, A., Gaviglio, J. and Dumas, R. (1967) "Structure of Velocity Space-Time Correlations in a Boundary Layer," Physics of Fluids Supplement, pp. S138-S145.

Hahn, M. (1976) "Turbulent Boundary-Layer Surface-Pressure Fluctuations Near an Airfoil Trailing Edge," AIAA paper 76-335.

Heidrick, T., Azad, R. S. and Banerjee, S. (1971) "Phase Velocities and Angle of Inclination for Frequency Components in Fully Developed Flow Through Pipes," Symposium on Turbulence in Liquids, Oct. 4-6, 1971, pp. 149-157.

Kiya, A., Sasaki, K. and Arie, M. (1982) "Discrete-Vortex Simulation of a Turbulent Separation Bubble," J. Fluid Mech., 120, pp. 219-244.

Klebanoff, P. (1954) "Characteristics of Turbulence in a Boundary Layer with Zero Pressure Gradient," NACA Report 1247.

Lahey, R. T. and Kline, S. J. (1968) "Representation of Space-Time Velocity and Pressure Fluctuations by a Tentative Phenomenological Model," Stanford Univ., Dept. Mech. Eng., Thermosciences Div. Report MD-22.

Lim, K. G. (1971) "A Study of Pressure Fluctuations in Turbulent Shear Flows Under the Effects of Mean Pressure Gradients," Thesis, Dept. Mech. Eng., Univ. Adelaide.

Mabey, D. G. (1972) "Analysis and Correlation of Data on Pressure Fluctuations in Separated Flow," J. Aircraft, 9, pp. 642f.

Mabey, D. G. (1982) "Comment on 'A Review of Research on Subsonic Turbulent Flow Attachment'," AIAA J., 20, pp. 1632f.

McGrath, B. E. and Simpson, R. L. (1987) "Some Features of Surface Pressure Fluctuations in Turbulent Boundary Layers with Zero and Favorable Pressure Gradients," NASA CR-4051.

Miller, J. (1976) "Simple Linearized Hot-Wire Anemometer," J. Fluids Engrg., 98, pp. 550-557.

Panton, R. L. and Linebarger, H. G. (1974) "Wall Pressure Spectra Calculations for Equilibrium Boundary Layers," J. Fluid Mech., 65, pp. 261f.

Perry, A. E. and Schofield, W. H. (1973) "Mean Velocity and Shear Stress Distribution in Turbulent Boundary Layers," Physics Fluids, 16, pp. 2068-2074.

Schloemer, H. H. (1967) "Effects of Pressure Gradients on Turbulent Boundary Layer Wall-Pressure Fluctuations," J. Acoustical Soc. Am., 42, pp. 93-113.

Schubauer, G. B. and Klebanoff, P. S. (1951) "Investigation of Separation of the Turbulent Boundary Layer," NACA Report 1030.

Shiloh, K., Shivaprasad, B. G. and Simpson, R. L. (1981) "The Structure of a Separating Turbulent Boundary Layer: Part 3, Transverse Velocity Measurements," J. Fluid Mech., 113, pp. 75-90.

Simpson, R. L. (1981) "A Review of Some Phenomena in Turbulent Flow Separation," J. Fluids Engrg., 103, pp. 520-533.

Simpson, R. L., Heizer, K. W. and Nasburg, R. E. (1979) "Performance Characteristics of a Simple Linearized Hot-Wire Anemometer," J. Fluids Engrg., 101, pp. 381-382.

Simpson, R. L. and Shivaprasad, B. G. (1983 b) "The Structure of a Separating Turbulent Boundary Layer: Part 5, Frequency Effects on Periodic Unsteady Freestream Flows," J. Fluid Mech., 131, pp. 319-399.

Simpson, R. L., Chew, Y.-T. and Shivaprasad, B. G. (1980) "Measurements of a Separating Turbulent Boundary Layer," Project SQUID Report SMU-4-PU; NTIS AD-A095 252/3.

Simpson, R. L., Shivaprasad, B. G. and Chew, Y.-T. (1981 a, b, c) "The Structure of a Separating Turbulent Boundary Layer; Part 1, Mean Flow and Reynolds Stresses; Part 2, Higher Order Turbulence Results," J. Fluid Mech., 113, pp. 23-74; Part 3, see Shiloh et al. (1981).

Simpson, R. L., Shivaprasad, B. G. and Chew, Y.-T. (1983) "The Structure of a Separating Turbulent Boundary; Part 4, Effects of Periodic Freestream Unsteadiness," J. Fluid Mech., 127, pp. 219-261.

Simpson, R. L., Strickland, J. H. and Barr, P. W. (1977) "Features of a Separating Turbulent Boundary Layer in the Vicinity of Separation," J. Fluid Mech., 79, pp. 553-594.

Stegen, G. R. and van Atta, C. W. (1970) "A Technique for Phase Speed Measurements in Turbulent Flow," J. Fluid Mech., 42, pp. 689-699.

Strickland, J. H. and Simpson, R. L. (1973) "The Separating Turbulent Boundary Layer: An Experimental Study of an Airfoil Type Flow," Thermal and Fluid Sciences Center Rept. WT-2, Southern Methodist University, AD-771170/8GA.

Thomas, A. S. and Bull, M. K. (1983) "On the Role of Wall Pressure Fluctuations in Deterministic Motions in the Turbulent Boundary Layer," J. Fluid Mech., 128, pp. 283-322.

Willmarth, W. W. (1958) "Space-Time Correlations of the Fluctuating Wall Pressure in a Turbulent Boundary Layer," J. Aero. Sci., 25, pp. 335f.

Willmarth, W. W. (1975) "Pressure Fluctuations Beneath Turbulent Boundary Layers," Annual Reviews of Fluid Mechanics, 7, pp. 13-38.

Wills, J. A. B. (1970) "Measurements of the Wavenumber/Phase Velocity Spectrum of Wall Pressure Beneath a Turbulent Boundary Layer," J. Fluid Mech., 45, pp. 65-90.

Standard Bibliographic Page

1. Report No. NASA CR-178309	2. Government Accession No.	3. Recipient's Catalog No.
4. Title and Subtitle AN EXPERIMENTAL STUDY OF SURFACE PRESSURE FLUCTUATIONS IN A SEPARATING TURBULENT BOUNDARY LAYER		5. Report Date June 1987
		6. Performing Organization Code
7. Author(s) R.L. Simpson, M. Ghodbane and B.E. McGrath		8. Performing Organization Report No.
9. Performing Organization Name and Address Aerospace and Ocean Engineering Department Virginia Polytechnic Institute and State University Blacksburg, VA 24061		10. Work Unit No. 505-61-51-06
		11. Contract or Grant No. NAG1-317
12. Sponsoring Agency Name and Address National Aeronautics and Space Administration Washington, DC 20546		13. Type of Report and Period Covered Contractor Report
		14. Sponsoring Agency Code

15. Supplementary Notes

Langley Technical Monitor: Thomas F. Brooks
Technical Report
R. L. Simpson and B. E. McGrath: Virginia Polytechnic Institute and State
   University, Blacksburg, Virginia.
M. Ghodbane: Southern Methodist University, Dallas, Texas.

16. Abstract

   Measurements of streamwise velocity fluctuation and surface pressure fluctuation spectra and wavespeeds are reported for a well-documented separating turbulent boundary layer. Because a portion of the acoustic pressure fluctuations is the same across the nominally two-dimensional turbulent flow, it is possible to decompose two microphone signals and obtain directly the turbulent flow contributions to the surface pressure spectra.

   The rms surface pressure fluctuation p' and spectra $\phi(\omega)$ increase through the adverse pressure gradient attached flow region and the detached flow zone and scale on the maximum turbulent shearing stress τ_M; p'/τ_M increases to the detachment location and decreases downstream due to the rapid movement of the pressure-fluctuation-producing motions away from the wall after the beginning of intermittent backflow.

   At lower frequencies for the attached flow $\phi(\omega) \sim \omega^{-0.7}$ while $\phi(\omega) \sim \omega^{-3}$ at higher frequencies. After the beginning of intermittent backflow, $\phi(\omega)$ varies with ω at low frequencies and ω^{-3} at high frequencies; farther downstream the lower frequency range varies with $\omega^{2.4}$. The surface pressure fluctuation celerity for the attached flow increases with frequency and agrees with the semi-logarithmic overlap equation of Panton and Linebarger. After the beginning of the separation process, the wavespeed decreases because of the oscillation of the instantaneous wavespeed direction and the streamwise coherence decreases drastically.

17. Key Words (Suggested by Authors(s)) turbulence separated flow boundary layers pressure fluctuations acoustics	18. Distribution Statement Unclassified - Unlimited Subject Category 71

19. Security Classif.(of this report) Unclassified	20. Security Classif.(of this page) Unclassified	21. No. of Pages 82	22. Price A05